

UC Santa Barbara

UC Santa Barbara Electronic Theses and Dissertations

Title

MIP-Coated Microbeam Mass Sensing Utilizing Noise Squeezing Effect in Parametric Resonance

Permalink

<https://escholarship.org/uc/item/2059j076>

Author

Li, Lily L.

Publication Date

2014

Peer reviewed|Thesis/dissertation

UNIVERSITY OF CALIFORNIA
Santa Barbara

MIP-Coated Microbeam Mass Sensing Utilizing
Noise Squeezing Effect in Parametric Resonance

A Thesis submitted in partial satisfaction of the
requirements for the degree of Master of Science

in

Mechanical Engineering

by

Lily Lijuan Li

Committee in Charge:

Professor Kimberly Turner, Chair

Professor Jeff Moehlis

Professor Sumita Pennathur

June 2014

The Thesis of Lily Lijuan Li is approved:

Professor Jeff Moehlis

Professor Sumita Pennathur

Professor Kimberly Turner, Committee Chairperson

May 2014

MIP-Coated Microbeam Mass Sensing Utilizing Noise Squeezing Effect in Parametric
Resonance

Copyright © 2014

by

Lily Lijuan Li

Acknowledgements

I would like to acknowledge my advisor Kimberly Turner for her patience and support. She has made herself available for individual meetings, which is always an enjoyable and productive time to discuss our progress, difficulties and goals. I would also like to thank Professor Sumita Pennathur and Professor Jeff Moehlis for being part of my committee.

It is my great pleasure to be part of the Turner MEMS group with wonderful colleagues. I appreciate Kamala Qalandar, Brian Gibson, Tobias Hiller, Mrigank Sharma, Jamie Booth for their friendship and help. I would also like to thank Zi Yie for his devices, Luke Shaw for his patience in helping me to get start with experimental work, Chris Burgner for his wisdom and inspiration, and Ellen Holthoff for coating my devices. Many thanks to Dave Bothman and clearroom staff for their guidance and support. Lastly, I would like to thank my family for always being there with love and generous support.

This work was supported by the Institute for Collaborative Biotechnologies under Grant W911NF-09-0001 through the U.S. Army Research Office. The content of the information does not necessary reflect the position or the policy of the Government and no official endorsement should be inferred.

The contents and figures in this thesis are reprinted with permission from Li, L., Holthoff, E.L., Shaw, L.A., Burgner, C.B., Turner, K.L. *Noise Squeezing Controlled Parametric Bifurcation Tracking of MIP-Coated Microbeam MEMS Sensor for TNT Explosive Gas Sensing*. IEEE/ASME Journal of IEEE, Microelectromechanical Systems. March 2014. (©2014 IEEE)

Curriculum Vitæ

Lily Lijuan Li

Education

- 2014 Master of Science in Mechanical Engineering, University of California,
Santa Barbara. GPA: 3.95/4.0
- 2012 Bachelor of Science in Mechanical Engineering, University of California,
Santa Barbara. GPA: 4.0/4.0

Experience

- 2012-Present Graduate Research Assistant at Turner MEMS Group
- 2014 Teaching Assistant, ME Design (ME 153)
- 2013 Teaching Assistant, Statics (ME 14)
- 2012-2013 Teaching Assistant, Senior Capstone Projects (ME 189)
- 2012 Teaching Assistant, Biomedical Devices (ME 128)
- 2012 Research Mentor, JKC Bridge Program at University of California,
Santa Barbara
- 2011 Summer Research Internship at Dr. Kimberly Turner's Lab
- 2011-2012 FEA Modeling of Beam Vibration for Energy Harvesting Project at
Dr. Jeff Moehlis's Research Group
- 2013 Advanced Vacuum Science Conference Poster Presentation, Long Beach,
CA

2014 Oral Presentation in Solid-State, Actuator, and Microsystems Workshop, Hilton Head, SC

Selected Publications

Li, L. L., Holthoff, E. L., Shaw, L. A., Burgner, C. B., Turner, K. L.:
“Noise Squeezing Controlled Parametric Bifurcation Tracking of MIP-Coated Microbeam MEMS Sensor for TNT Explosive Gas Sensing,”
Journal of Microelectromechanical Systems, (Volume: PP , Issue: 99),
March 2014

Li, L. L., Holthoff, E. L., Shaw, L. A., Burgner, C. B., Turner, K. L. :
“Phase Noise Squeezing Based Parametric Bifurcation Tracking of MIP-Coated Microbeam MEMS Sensor for TNT Explosive Gas Sensing,” in Solid-State Sensor, Actuator, and Microsystems Workshop, Hilton Head Workshop, 2014

Abstract

MIP-Coated Microbeam Mass Sensing Utilizing Noise Squeezing Effect in Parametric Resonance

by

Lily Lijuan Li

A real-time explosive gas sensing (DNT) in atmospheric pressure utilizing the noise squeezing effect that occurs before a bifurcation event is investigated. A noise-squeezing controller based on the statistics of phase noise is implemented using high-speed LabVIEW field programmable gated array. A high frequency TNT-molecularly imprinted fixed-fixed microbeam sensor utilizes this nontraditional sensing strategy and performs DNT sensing at various concentrations. Experiments are conducted using both noise-based and sweep-based bifurcation tracking for a direct comparison. Results demonstrate noise-based bifurcation tracking is not only capable of performing reliable frequency tracking, but also show the method is superior to the bifurcation sweep-based tracking. Over three orders of magnitude improvement in acquisition rate is achieved, and as a result, confidence and precision on bifurcation frequency estimation is significantly improved over the bifurcation sweep tracking method, enabling DNT sensing at concentrations much below sub-ppb (parts-per-billion) level.

Contents

| | |
|---|-----------|
| Acknowledgements | iv |
| Curriculum Vitæ | vi |
| Abstract | viii |
| List of Figures | xi |
| List of Tables | xv |
| 1 Introduction | 1 |
| 1.1 Overview | 1 |
| 1.2 Cantilever in Sensing | 3 |
| 1.3 Harmonic Resonance Mass Sensing | 3 |
| 1.4 Parametric Mass Sensing | 5 |
| 1.5 Sweep Based Parametric Mass Sensing | 7 |
| 1.6 Noise Squeezing Based Mass Sensing | 10 |
| 1.7 Effect of Damping in Parametric Resonance | 12 |
| 2 Device Fabrication and Characterization | 15 |
| 2.1 Device Fabrication | 15 |
| 2.2 Device Functionalization | 17 |
| 2.3 Natural frequency | 19 |
| 3 Experimental Setup and Controller Design | 20 |
| 4 Results | 24 |
| 5 Discussion | 32 |
| 6 Conclusion | 35 |

| | | |
|----------|--|-----------|
| 7 | Future Work | 37 |
| 7.1 | Choice of Control Locations | 37 |
| 7.2 | Implementation of PI controller and its limitation | 39 |
| | Bibliography | 42 |
| | Appendices | 49 |
| A | Fabrication Of Fixed-Fixed Beams | 50 |
| A.1 | Recipe I | 50 |
| A.2 | Recipe II | 54 |
| B | DNT Concentration Calculation | 58 |
| C | Method of Averaging and Steady State Solution | 60 |

List of Figures

| | | |
|-----|---|---|
| 1.1 | Bottom: Schematic of stability transition curve (black). The blue lines symbolize the amplitude R at constant voltage. Solid blue lines are stable solutions, dashed blue lines are unstable ones. Top: Phase diagrams of the amplitude for each of the three regions. The red dot indicates the point of operation of the feedback controller, that in turn tracks the shift to the left and the right of the transition curve induced by change in mass [1][2]. | 6 |
| 1.2 | Illustration of forcing applied to a cantilever to achieve parametric resonance. The fixed-fixed beam is driven at \sim twice its natural frequency (ω). When driven above the threshold of the Arnold tongue, a subcritical/supercritical bifurcation results at ω | 7 |
| 1.3 | (a) and (b) corresponds to the amplitude and phase response in linear mass sensing. The blue and red curves represent the system response before and after mass loading. (c) describes the Arnold tongue correspondence to the natural frequency before and after mass absorption. Δf is the change of frequency. B is the bifurcation location where the jump event occurs [3]. . . | 8 |
| 1.4 | Schematic of both noise squeezing-based tracking (left) and bifurcation sweep-based tracking methods (right). The bifurcation sweep based tracking method tracks the bifurcation locations by repeatedly performing frequency sweeps towards critical point until large amplitude results. Then the device is relaxed to a zero stable state before the next sweep starts. However, in the noise squeezing control tracking method, the device approaches the critical point until the noise squeezes below some threshold, then a feedback control keeps the device close to the edge of instability while maintaining small a response amplitude. Note that voltage can be used as a control parameter instead of frequency to map the bifurcation location as well, but it is not demonstrated in this work. | 9 |

| | | |
|-----|--|----|
| 1.5 | Transient Response of a parametrically excited gyro before and after the critical bifurcation point. A coordinate transformation of (q_1, q_2) into a frame rotating at half the drive frequency is used. The system undergoes a subcritical pitchfork bifurcation. Far away from the critical point, the phase (in red) alternates randomly with a large variance. As the device approaches the critical point, indicated by the transition from red to green, the dynamics collapse onto a one dimensional slow manifold, where the phase variance drops dramatically, making it an ideal location for control. As a consequence, the phase noise correlates and the amplitude starts to grow. Escape to a large amplitude (in purple) occurs as the parameters cross the instability boundary [4]. Note that this figure is used for the purpose of illustration; it does not represent the actual system of the device under test in this work, but a similar one. | 11 |
| 1.6 | Effect of damping in parametric resonance system. Without damping, the tip of the tongue is very sharp, and theoretically, any nonzero forcing can drive the device into the nonlinear region inside the tongue. With damping, the bottom of the tongue is rounded, and a higher actuation force is required to achieve parametric resonance. However, damping does not affect the sharpness of the bifurcation event, nor does it affect the slope of the instability edges at higher forcing strengths. | 14 |
| 2.1 | Fabrication process schematics of the fixed-fixed beams using standard SOI process. (a) SiN and SiO ₂ is deposited on backside of SOI wafer as a mask for KOH backside etch in step (h). (b) Front side lithography with photoresist to pattern the beam features. (c) Dry etch silicon with deep reactive ion etching (DRIE). (d) Back side lithography with second mask align to front side pattern. (e) Dry etch SiN and SiO ₂ induction coupled plasmas etcher (ICP). (f) Spin coat ProTEK on front side as protection during back side etching. (g) KOH etch back side until reaching buried oxide layer. (h) Remove ProTEK and HF etch buried oxide to release devices [3]. | 16 |
| 2.2 | SEM image of a 450 μm x 20 μm x 2 μm sensor coated with MIPs [3]. | 18 |

3.1 Experimental setup and FPGA controller design schematics. The device is mounted onto a shear piezo and is driven at twice its natural frequency. The sensor's out of plane velocity response is coupled by a laser vibrometer through an optical microscope. The vibrometer signal and the reference square wave at half the drive frequency are fed into a phase lock amplifier (PLA). The FPGA samples the outputs of the PLA and provides feedback control to hold response close to the edge of bifurcation. The 2-4 DNT/N₂ gas test experiment is conducted in a closed chamber at atmospheric pressure and room temperature. DNT/N₂ is generated by heating the 2-4 DNT permeation tube in a permeation oven at constant temperature. DNT vapor is carried by N₂ and the mixture is fed into the test chamber at constant flow rate controlled by mass flow controllers. When the device is not under active DNT test, only N₂ is used.

21

4.1 Sensor response to noise squeezing controller. Fig.4.1(a) shows the response of the sensor when noise squeezing controller is in action. When the sensor is away from the edge of instability, the phase is varying between $-\pi$ and π , and that corresponds to the zero stable solution of the supercritical pitchfork bifurcation. As the device approaches the edge of bifurcation, phase squeezes and amplitude starts to grow. When phase variance goes below threshold, the controller brings the sensor back to the stable state. Such process repeats and the time between one squeeze state and the next is less than 10 ms. Fig.4.1(b) is the phase variance data blow up of the highlighted portion in red in Fig.4.1(a). Minimum variance is found to be 0.002. This corresponds to the variance set point at which a feedback control was employed by adjusting the drive frequency to keep the device getting too close to the escape event.

25

4.2 The figure shows a constant concentration of 0.93 ppb DNT/N₂ gas experiment. Pure N₂ was first introduced for 15 minutes and was followed 10 minutes of DNT/N₂. The parametric drive frequency was lowered by 67 ± 3 Hz due to the polymer absorption of DNT. The same process was repeated 9 times. The linear frequency drift of 0.05 Hz/min was accounted for in the post processing.

26

4.3 DNT gas sensing using a noise squeezing controller. Fig.4.3 (a) shows the gas experiment with lowest concentration of 1.38 ppb and highest concentration of 18.13 ppb. Fig.4.3(b) is a zoom in figure of the portion inside the square window in Fig.4.3(a). The highlighted portion corresponds to pure N₂ purging after the 1.38 ppb DNT/N₂ gas test. However, absorbed DNT did not completely come off, and the frequency did not fully recover initial starting frequency. Hence, this explains why the highlighted data in red does not start at zero. Fig.4.3 (b) is used to make direct comparison with the data collected from the bifurcation sweep method (Fig.4.4) at the same concentration. . . .

27

| | |
|---|----|
| 4.4 Comparison test showing DNT gas sensing using the bifurcation sweep method. Pure N ₂ was introduced after the first and last DNT gas test (2.03 ppb and 10.88 ppb). Absorption phenomenon persisted, and the following higher concentration DNT/N ₂ experiments were conducted after the steady state of lower concentration was reached. | 28 |
| 4.5 Calibration of DNT plotted with change of frequency as a function of DNT concentration using both tracking methods. The slope corresponds to sensitivity in units of Hz/ppb. The error bar is not shown in the figure, as it is invisible in the plot using the plot dot size shown. | 29 |
| 4.6 Transition from DNT gas testing to pure N ₂ . Fig.4.6 (a) shows the 1.38 ppb DNT tracking using the noise squeezing controller and sharper transition is observed compared to the bifurcation sweeping method of 2.03 ppb in Fig.4.6 (b). Note that concentration is different in this figure; however, the focus on this result is not the frequency shift but the sensor response to the environmental change when switching the control valves on and off. Hence, the comparison is still valid despite being two different concentration tests. . | 31 |
| 7.1 Control locations inside the Arnold Tongue. Point A and B are possible control set points. A is closer to the transition location where zero instability changes. At this point, the amplitude response along the bistable branch is steeper, which is likely to be more sensitive. B is further inside the tongue at a large amplitude, this location is less steep, but easier to control [2][1]. . . . | 38 |
| 7.2 Illustration of how control set point A and B moves with the bistable branch in mass sensing experiment. Red and blue curve represent after and before mass absorption respectively. | 38 |
| 7.3 Water vapor experiment. <i>Top:</i> The controller actively controls the amplitude at set point (in red) by modulating the drive frequency. <i>Bottom:</i> When water vapor is introduced, natural frequency change of the sensor cause a shift of the tongue, and thus the stable branch. By controlling constant amplitude, the change in frequency is traced by the controller simultaneously. The change in mass Δm is directly related to Δf . The water vapor experiment is conducted by alternating water vapor and N ₂ purging cycles. Reversibility and repeatability are demonstrated [2]. | 40 |

List of Tables

| | |
|--|----|
| 4.1 Comparison of the two nonlinear tracking methods. This table summarizes the results of both the noise squeezing-based and bifurcation sweep-based methods. Minimum frequency corresponds to the Allan Variance for each method and the sensitivity relates to the slope of the calibration curve. LOD is the ratio between the minimum frequency and the sensitivity | 30 |
| B.1 Specifications of 2-4 DNT permeation tube. | 58 |
| B.2 Concentrations of DNT and its corresponding temperature and flowrate settings. | 59 |

Chapter 1

Introduction

1.1 Overview

High sensitivity and selectivity and low cost are key considerations for trace explosive detection sensors [5]. Commercially available explosive detection systems can detect with a mass sensitivity in the range of pg to ng, however, these equipments are usually large, some are up to a few hundred pounds, hence, not feasible for detection of explosives on sites of interests. In addition, some of them are slow and expensive [6]. Low mass, high frequency and low cost micro/nano sensors, commonly known as microelectromechanical systems (MEMS) have draw increasing attention in the area of mass sensing in recent years [7][8]. The smallness of these sensors enables the detection of molecules in vapors, making it a very prominent technology in the field of trace detection, especially in the area of explosive detection for homeland security. Silicon fabricated MEMS sensors themselves do not have the capability of mass sensing, hence, a surface modification combining with novel coating that demonstrated high affinity and

selectivity to target molecules can be employed to activate the sensing ability of the devices. In this project, we are collaborating with scientists from the Army Research Laboratory (ARL) who are working on a coating chemistry called molecular imprinted polymers (MIPs). MIPs have become an attractive thin-film coating for many MEMS sensors, and a deeper understanding of binding sites in MIPs has been achieved [9][10]. In this work, ~ 15 nm-thick films of sol-gel-derived xerogels molecularly imprinted for trinitrotoluene (TNT) have demonstrated selectivity and stability in combination with a fixed-fixed beam MEMS sensor [11][12]. Traditionally, mass sensing using MEMS has been achieved based on the natural frequency shift due to an increase of resonator mass. However, thermomechanical noise has determined the limit of detection for linear sensing [13]. The ability to track the minimum shift of the natural frequency is determined by both the intrinsic and extrinsic noise of the system. Dynamics of parametrically excited oscillators and their applications have been previously studied extensively [14][15][16]. Successful attempts to improve the effective quality factor of microcantilever arrays operating in the linear regime utilizing parametric amplification have been made [17] [18] [19]. However, bifurcation mass sensing has demonstrated superior sensitivity in the presence of measurement noise when compared to linear sensing in air [20].

1.2 Cantilever in Sensing

The microcantilever is one of the most commonly known resonant structures in MEMS used in the area of physical and chemical sensing. For example, the atomic forced microscope tip is basically a cantilever [21]. The smallness of these MEMS devices offers high sensitivity that allows measurement down to 0.1 Å. In the area of sensing, mass added to the cantilever can be measured by its deflection [22][23] or surface stress [24][25]. A popular way to do it is to operate the cantilever at its harmonic resonant mode and measure its frequency shift as a result of mass loading. Resonant sensing can be done in the linear harmonic region [5][26] and the nonlinear harmonic region [27][16]. In this work, we are interested in exploiting nonlinearity in MEMS cantilevers and apply it in mass sensing.

1.3 Harmonic Resonance Mass Sensing

Linear harmonic resonance mass sensing is based on the natural frequency shift of the MEMS device when particles are attached to the surface (Fig.1.3 (a) and (b)). The dynamics of the microcantilever can be modeled as a mass spring damper system:

$$m\ddot{x} + c\dot{x} + kx = F(t), \tag{1.1}$$

where m is the mass, c is damping, and k is spring stiffness, and F is the forcing. Natural frequency of the harmonic oscillator is:

$$f_0 = \frac{1}{2\pi} \sqrt{\frac{k}{m}}, \quad (1.2)$$

The addition of mass is directly related to the change of the harmonic frequency. Assume the added mass Δm is small and the stiffness change can be ignored, then the new frequency f can be expressed as:

$$f = \frac{1}{2\pi} \sqrt{\frac{k}{m + \Delta m}}, \quad (1.3)$$

Performing a Taylor expansion on Eq.1.2 with Δm being very small, we get an approximate relationship between the frequency change and added mass as follows [28]:

$$\Delta f = -\frac{1}{2} \frac{\Delta m}{m} f_0 \quad (1.4)$$

As seen in Eq.1.4, improving the frequency sensitivity ultimately leads to a lower order of mass detection limit. Improving the quality factor (Q factor) by utilizing parametric pumping improves the frequency resolution in linear sensing [17], however, previous work showed that nonlinear sensing offered higher frequency resolution in the presence of measurement noise [20].

1.4 Parametric Mass Sensing

In the context of this work, we consider the nonlinear sensing of a cantilever operating near/at its parametric resonance. Parametric sensors operate by periodically modulating the effective stiffness of the system [29]. The dynamics of the resulting system is governed by the Mathieu equation with a cubic nonlinearity [29].

$$m\ddot{y} + c\dot{y} + (k + \nu \cos 2\omega t)y + k_3y^3 = 0, \quad (1.5)$$

where m is the mass, c is the damping coefficient, k is the spring stiffness and is being periodically modulated by a sinusoidal input with strength ν , and k_3y^3 is the cubic nonlinearity term. The above equation can be derived by calculating the total kinetic energy (T) and potential energy (V) of the system and applying them in the Lagrange's equation [30] [3]:

$$\frac{d}{dt}\left(\frac{\partial T}{\partial \dot{y}}\right) - \frac{\partial T}{\partial y} + \frac{\partial V}{\partial y} = -c\dot{y} \quad (1.6)$$

The solution to Eq.1.5 is solved using the method of averaging [31]. See Appendix C for detailed derivation of steady state solutions. The dynamic response is illustrated by Fig.1.1. When operated above the threshold voltage determined by mapping the Arnold tongue [32] that defines the stable and unstable regions, a subcritical/supercritical pitchfork bifurcation results, depending on the parameter sweep direction. As shown in Fig.1.1, the boundary that defines the change of stability of the system is called the Arnold tongue. Outside the Arnold tongue, zero is always a stable solution. For a

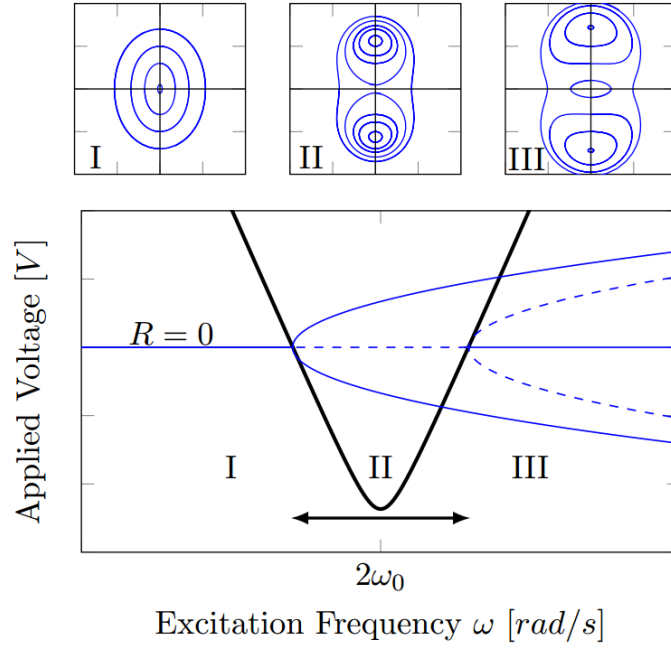


Figure 1.1: Bottom: Schematic of stability transition curve (black). The blue lines symbolize the amplitude R at constant voltage. Solid blue lines are stable solutions, dashed blue lines are unstable ones. Top: Phase diagrams of the amplitude for each of the three regions. The red dot indicates the point of operation of the feedback controller, that in turn tracks the shift to the left and the right of the transition curve induced by change in mass [1][2].

hardening case (Fig.1.1), on the right hand side of the Arnold tongue, there exist two large stable solutions and one zero stable solution. Inside the tongue, zero becomes unstable and two large stable solutions are born.

The effective stiffness modulation can be achieved by relying on the nonlinear actuation force produced by non-interdigitated combs [33] or by gap varying shaped combs [34]. In this work, the effective stiffness is modulated by applying a periodic voltage (to an external shear piezo), which is equivalent to applying a periodic forcing in the axial direction of the cantilever beam, as illustrated in Fig.1.2. The parameters in Eq.1.5

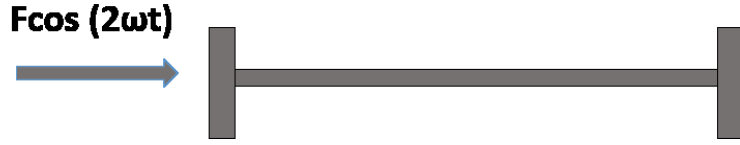


Figure 1.2: Illustration of forcing applied to a cantilever to achieve parametric resonance. The fixed-fixed beam is driven at \sim twice its natural frequency (ω). When driven above the threshold of the Arnold tongue, a subcritical/supercritical bifurcation results at ω .

can be determined by applying curve fitting to the experimental data. Damping (c) and forcing strength (ν) can be obtained from mapping the Arnold tongue. The cubic nonlinearity k_3 can be obtained from the transition curve (bistable branch inside the Arnold tongue) [1]. When frequency is swept from right to left in Fig.1.1, large amplitude jumps of the system occur when crossing the instability boundary (Fig. 1.4), where the drive frequency is approximately twice the system's natural frequency [35].

In contrast to linear mass sensing (Fig.1.3 (a) and (b)), bifurcation mass sensing utilizes the occurrence of the jump event as an on/off indication of the bifurcation location to directly relate it to the natural frequency of the system. As a result, natural frequency shifts due to mass loading can be traced by tracking the shifts in bifurcation location (Fig.1.3), since a corresponding shift of frequency is observed in the instability boundary (Arnold Tongue).

1.5 Sweep Based Parametric Mass Sensing

For bifurcation tracking-based mass sensing, the frequency is swept towards the critical point. Note that voltage can be varied to achieve bifurcation as well, as seen in

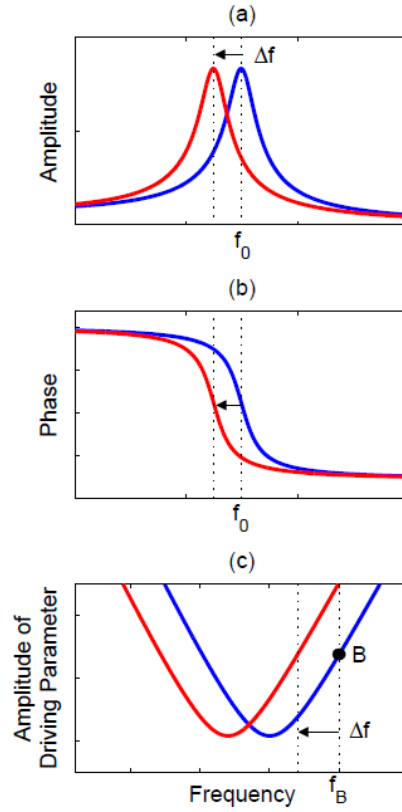


Figure 1.3: (a) and (b) corresponds to the amplitude and phase response in linear mass sensing. The blue and red curves represent the system response before and after mass loading. (c) describes the Arnold tongue correspondence to the natural frequency before and after mass absorption. Δf is the change of frequency. B is the bifurcation location where the jump event occurs [3].

Fig.1.4. However, it is more sensible to sweep frequency due to its direct correlation to mass change. Once the system response amplitude crosses a set threshold, the location of the bifurcation is found, and the sensor is reset to a low amplitude (zero solution stable state) state. Frequency sweep then restarts to find the next bifurcation point (shown in green in Fig.1.4). Precise frequency estimation in micromechanical parametric oscillators can be achieved by statistics of multiple bifurcation events acquired with

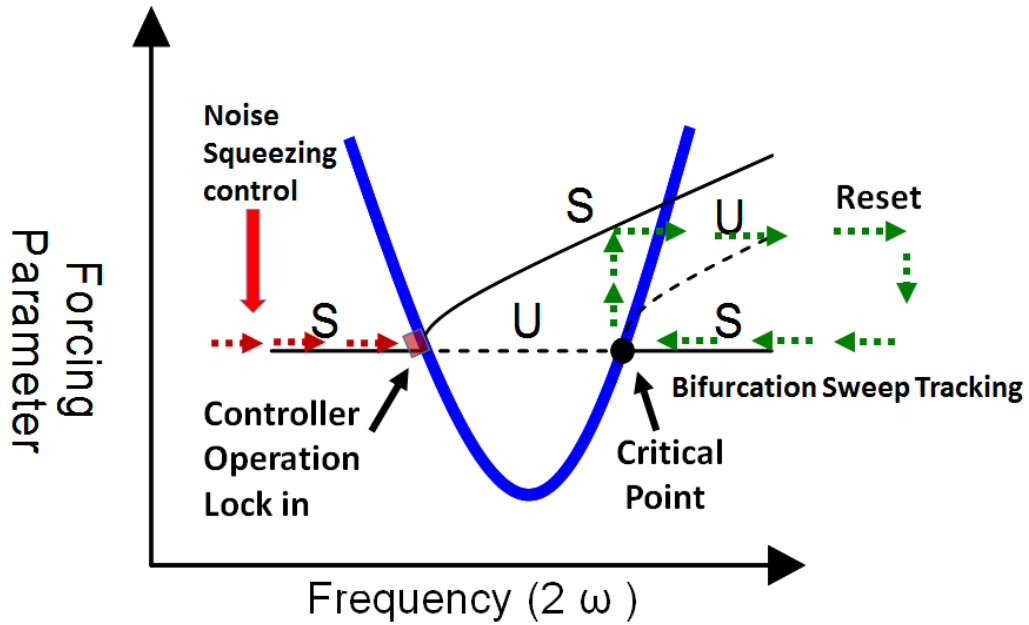


Figure 1.4: Schematic of both noise squeezing-based tracking (left) and bifurcation sweep-based tracking methods (right). The bifurcation sweep based tracking method tracks the bifurcation locations by repeatedly performing frequency sweeps towards critical point until large amplitude results. Then the device is relaxed to a zero stable state before the next sweep starts. However, in the noise squeezing control tracking method, the device approaches the critical point until the noise squeezes below some threshold, then a feedback control keeps the device close to the edge of instability while maintaining small a response amplitude. Note that voltage can be used as a control parameter instead of frequency to map the bifurcation location as well, but it is not demonstrated in this work.

small frequency sweep steps [36]. However, the bifurcation tracking method is highly dependent on a parameter α , defined as sweep rate to noise ratio [37]. If the sweep rate is too slow, noise activated escape can occur where the bifurcation occurs before the critical point is reached [38][39]. On the other hand, if the sweep rate is too fast, delay bifurcation can result where bifurcation occurs after the critical point [40][41]. Even though an optimum α can be chosen for an experiment, that particular sweep rate may not offer the acquisition speed needed for acceptable sensor performance.

1.6 Noise Squeezing Based Mass Sensing

The noise squeezing effect in parametrically excited system was first demonstrated in [19]. Recent work on parametric noise squeezing and parametric resonance of microcantilever utilizing feedback control has shown significant improvement in the effective quality factor, opening the field to high sensitivity mass sensing even in liquid environment [42]. A similar sensing strategy based on phase noise for fast estimation of bifurcation location has been developed and verified with a low frequency MEMS gyroscope as seen in [43][44][45]. The phase squeezing effect is explained in Fig.1.5. It demonstrates the dynamic behavior of the device before and after the bifurcation event. Far away from the pitchfork bifurcation (in red), the zero-fixed point of the system is stable and the phase space appears random with a large variance. As the device approaches the critical point, the system dynamics collapse onto a slow manifold, where the amplitude response of the system started to grow, but remains small (as shown in Fig.1.5 where the transition varies from red to green). The slow manifold corresponds to the system eigenvector associated with the eigenvalue with small magnitude. The time scale that governs the slow manifold is much slower than the natural frequency of the oscillator. As the zero state loses its stability, the resulting motion moves along the slow manifold to one of the newly formed large amplitude stable fixed points (in purple) [4]. The change in phase variance is obvious just prior to the critical point; hence, this squeezing state can be used as a precursor to the bifurcation event. A feedback

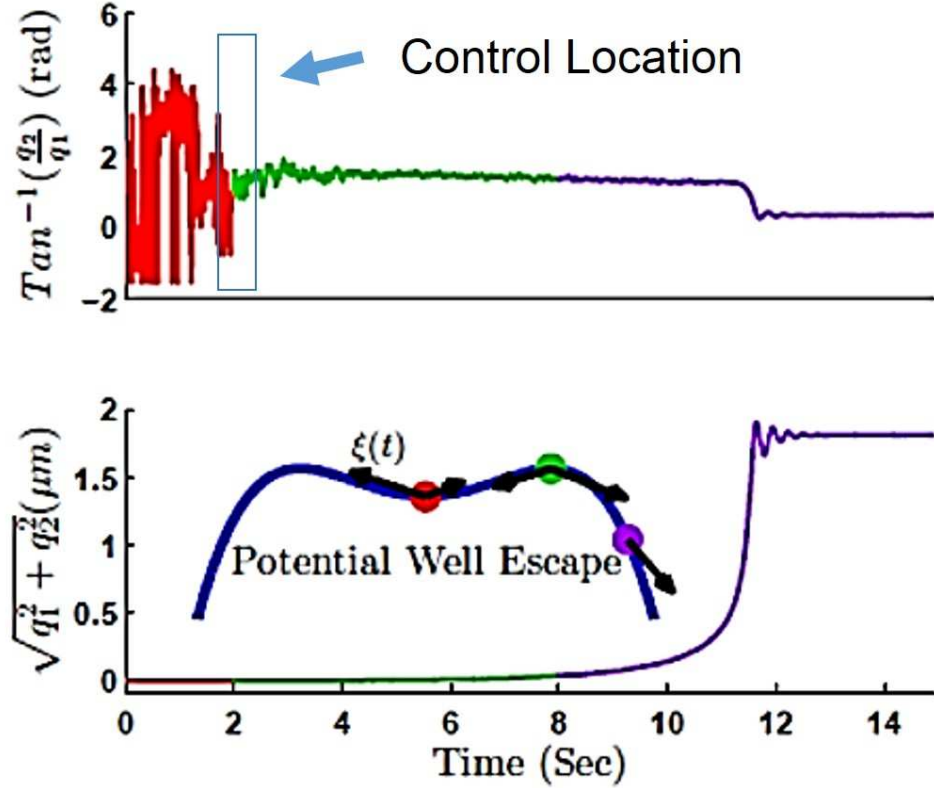


Figure 1.5: Transient Response of a parametrically excited gyro before and after the critical bifurcation point. A coordinate transformation of (q_1, q_2) into a frame rotating at half the drive frequency is used. The system undergoes a subcritical pitchfork bifurcation. Far away from the critical point, the phase (in red) alternates randomly with a large variance. As the device approaches the critical point, indicated by the transition from red to green, the dynamics collapse onto a one dimensional slow manifold, where the phase variance drops dramatically, making it an ideal location for control. As a consequence, the phase noise correlates and the amplitude starts to grow. Escape to a large amplitude (in purple) occurs as the parameters cross the instability boundary [4]. Note that this figure is used for the purpose of illustration; it does not represent the actual system of the device under test in this work, but a similar one.

controller based on the phase variance can therefore be implemented to keep the device at the edge of instability (Fig.1.4).

Using the statistics of the phase noise to estimate the bifurcation location leads to over three orders of magnitude improvement in acquisition rate when compared with the frequency sweep based bifurcation-tracking method. These results [42][43][44][45] imply potential applications in improving sensitivity of mass sensing using MEMS, but no one has yet fully taken advantage of this sensing strategy and combined it with real time mass sensing. In this work, a noise-squeezing controller implemented on National Instrument LabVIEW CompactRIOTM platform consisting of a field programmable gated array (FPGA) was combined with a high frequency molecularly imprinted (for TNT) fixed-fixed microcantilever to perform real time dinitrotoluene (DNT) gas sensing experiments. To demonstrate the advantages of noise squeezing controlled bifurcation tracking, we conducted experiments using both noise squeezing-based and sweep-based bifurcation tracking as described in [12]. Results showed that the noise squeezing sensing strategy led to a significant improvement in acquisition rate and frequency stability, both being crucial for improving the sensitivity of MEMS mass sensors.

1.7 Effect of Damping in Parametric Resonance

In harmonic resonance, damping significantly reduces the quality factor and hence, lowers the mass sensitivity in the application of mass sensing. As a result, various techniques are employed to improve the quality factor when operating the sensor in

atmospheric pressure using harmonic resonance tracking. One example of quality factor enhancement is parametric amplification [17]. However, when operating the device in parametric resonance mode, damping does not hinder the performance as much compared to linear harmonic sensing. The effect of damping is reflected on the tongue shape, as shown in Fig. 1.6. Without damping, the tip of the tongue is very sharp, and any nonzero forcing can drive the device into the nonlinear region inside the tongue. In a damped environment, the bottom of the tongue is rounded, and a higher actuation forcing is required to achieve parametric resonance. However, damping does not affect the sharpness of the bifurcation jumps, nor the slope of the instability edges at high forcing strengths. Hence, one can still track the tongue with high accuracy in the presence of damping, which makes the parametric resonance sensing ideal for mass sensing in atmospheric pressure.

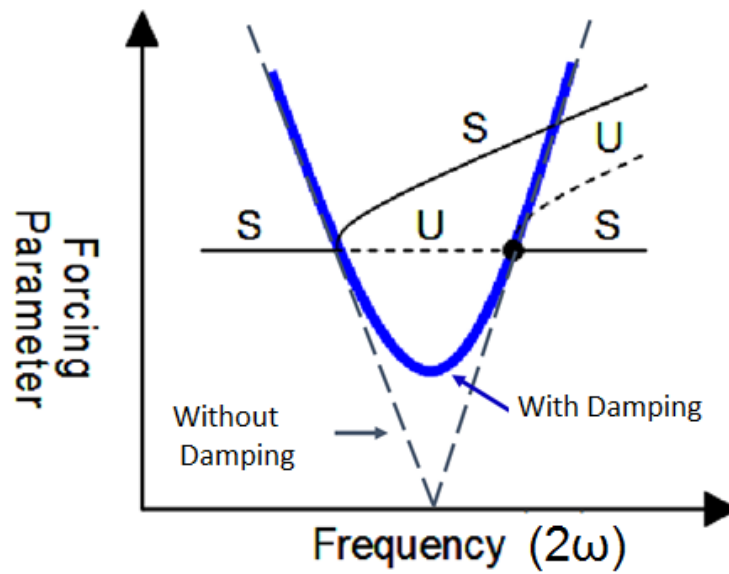


Figure 1.6: Effect of damping in parametric resonance system. Without damping, the tip of the tongue is very sharp, and theoretically, any nonzero forcing can drive the device into the nonlinear region inside the tongue. With damping, the bottom of the tongue is rounded, and a higher actuation force is required to achieve parametric resonance. However, damping does not affect the sharpness of the bifurcation event, nor does it affect the slope of the instability edges at higher forcing strengths.

Chapter 2

Device Fabrication and Characterization

2.1 Device Fabrication

The sensors are fixed-fixed beams of varied lengths and widths. The beam thickness was $2\ \mu\text{m}$. The values were chosen so that the natural frequencies of the beams were less than half the natural frequency of the shear piezo actuator (330 kHz) used to drive device. The microbeams were fabricated using a standard SOI process (Fig.2.1) [3].

The SOI wafer used was $2\ \mu\text{m}$ Si device layer with $1\ \mu\text{m}$ buried oxide and $520\ \mu\text{m}$ Si handle. First, oxide was grown on both sides of the wafer. Si_3N_4 was deposited on the backside on top of silicon oxide; together they serve as masks to protect the backside for KOH etch in a later step [Fig.2.1 (a)]. After front side oxide removal, it was then spun with photoresist and pattern was transferred [Fig.2.1 (b)]. Then a deep reactive-ion etching was used to etch the device features [Fig.2.1 (c)]. Backside mask features were defined using photolithography and inductively coupled plasma

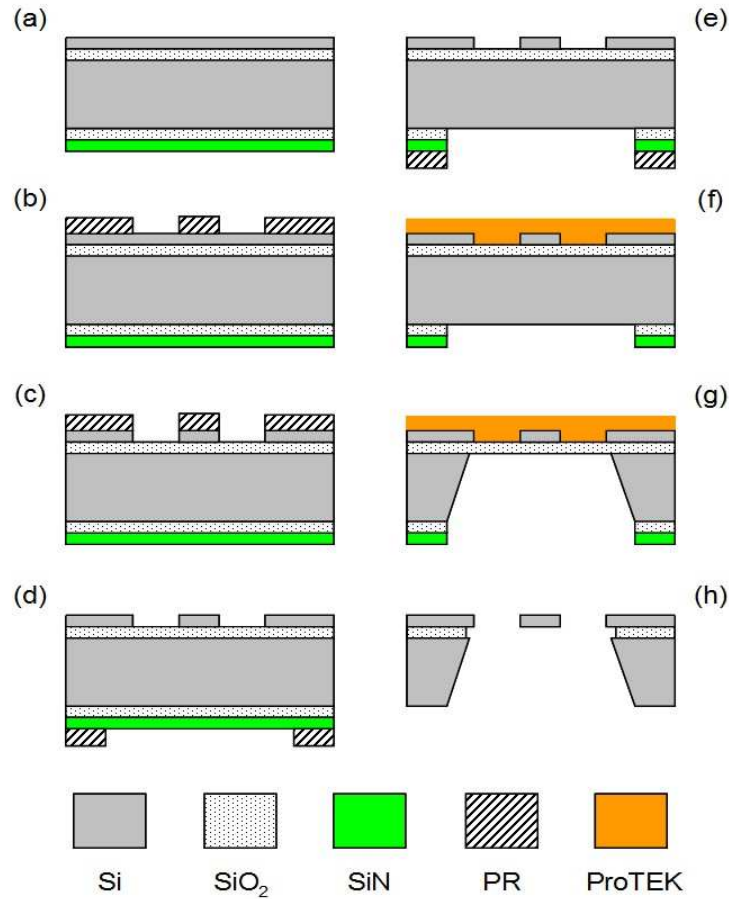


Figure 2.1: Fabrication process schematics of the fixed-fixed beams using standard SOI process. (a) SiN and SiO₂ is deposited on backside of SOI wafer as a mask for KOH backside etch in step (h). (b) Front side lithography with photoresist to pattern the beam features. (c) Dry etch silicon with deep reactive ion etching (DRIE). (d) Back side lithography with second mask align to front side pattern. (e) Dry etch SiN and SiO₂ induction coupled plasmas etcher (ICP). (f) Spin coat ProTEK on front side as protection during back side etching. (g) KOH etch back side until reaching buried oxide layer. (h) Remove ProTEK and HF etch buried oxide to release devices [3].

[Fig.2.1 (d) and (e)]. The front side was spun with protected coating called ProTEK to protect features during backside release etch [Fig.2.1 (f)]. The backside was opened by anisotropic KOH etch and stopped at the buried oxide. The device was then finished with removal of ProTEK and buried oxide layer [Fig.2.1 (g) and (h)]. KOH etch rate is

highly dependent on parameters such as temperature, agitation, concentration, etc. It is easy to under/over etch the backside. The fact that the proTEK peels off when the wafer is taken out of the KOH (to check the etch depth) makes this wet etching less desirable. An easier process to fabricate fixed-fixed beams was also developed. Instead of using ProTEK and KOH to etch the backside, DRIE dry etch can be used to etch away 500 μm of Si and stop at the buried SiO_2 . This results in a more controllable backside etching. Detail on the fabrication processes can be found in Appendix A.

2.2 Device Functionalization

Molecular imprinted polymer (MIP) is a product of the molecular imprinting technology. It involves an initial polymerization between functional monomers and template, then the removal of the template, formation of a cavity in the polymer which has a “memory” and affinity for the template molecule. They can be used as robust artificial recognition elements for target chemical analytes of interest. Their physicochemical properties can be adjusted by the choice of functional monomers. In this work, xerogel-based MIPs were used for coating. The MIP used was a combination of 3-aminopropyltriethoxysilane (APTES), methyl-triethoxysilane (C1-TriEOS), and 3-mercaptopropyl trimethoxysilane (MPTMS). This integrated MIP has shown that it is selective to TNT and has demonstrated reliable reversibility and stability. It was expected to maintain its selective properties for at least six months [11]. The devices were spin-coated with the xerogel-based MIPs, a coating method that was found to offer

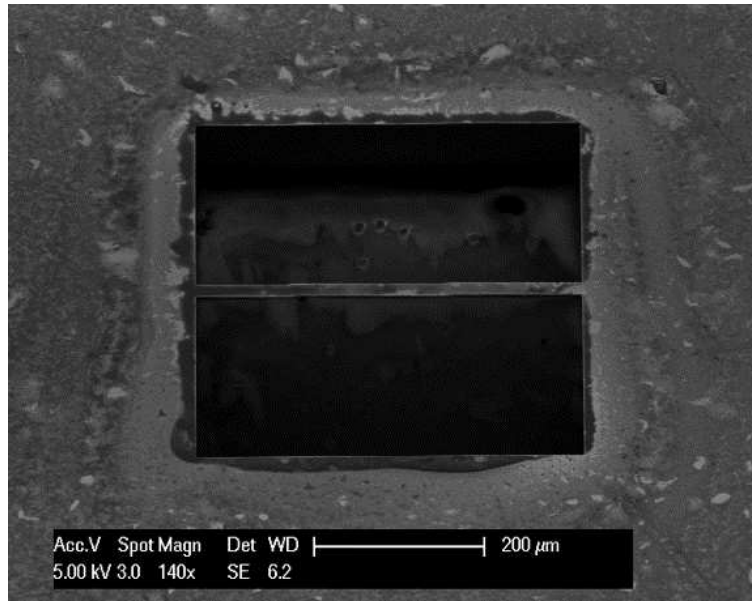


Figure 2.2: SEM image of a $450 \mu\text{m} \times 20 \mu\text{m} \times 2 \mu\text{m}$ sensor coated with MIPs [3].

the best results compared with microdrop deposition. Fig.2.2 shows an SEM image of a microsensor spin-coated with MIPs [3]. Note that the MIPs were developed to detect TNT, however, DNT, a chemical precursor to TNT, was used in the experiments conducted in this work. Conclusions drawn from the results of DNT testing will be similar to TNT since they are structurally similar. Devices described here are the same as those used to compare bifurcation tracking to natural frequency tracking of DNT in [12]. Results successfully demonstrated the capability of microbeam sensor detecting DNT with a limit of detection (LOD) in the sub-ppb range using the bifurcation sweep tracking method. Note that the sensors were coated and last tested in September 2011. They were later introduced to DNT gas sensing with noise squeezing controller for bifurcation sensing in May 2013. One drawback to MIPs is their stability after aging. This particular MIP displayed resistance to this degradation. Nearly two years of idling

can degrade the effectiveness of the polymers, which is addressed in the results section. The sensor used in this work is $600 \mu m \times 20 \mu m \times 2.462 \mu m$ with a natural frequency of 49.33 kHz.

2.3 Natural frequency

The natural frequency of the fixed-fixed beam can be calculated from the following equation:

$$f_n = 1.03 \frac{h}{L^2} \sqrt{\frac{E}{\rho}}, \quad (2.1)$$

where h is the thickness of the beam, L is the length, E is the Young's Modulus of [1 0 0] silicon (130 GPa) and ρ is density of silicon (2650 kg/m^3). Substituting the dimensions of the beams from the previous section, a natural frequency of 49.336 kHz is obtained from Eq.2.1.

Chapter 3

Experimental Setup and Controller Design

Theory and an earlier proof of concept experiment on a low frequency MEMS with a fundamental frequency of 8448 Hz showed that phase noise squeezes onto the slow manifold prior to the bifurcation event. The statistics of the phase noise squeezed state can be used as a precursor to the critical location [40][41][43]. Taking advantage of this sensing method, we implemented it on a TNT-molecularly imprinted sensor with a natural frequency of 49.33 kHz. The experimental setup is shown in Fig.3.1.

The sensor was mounted on a shear piezo, driven by the function generator at nearly twice the resonant frequency (to drive parametric resonance) at a fixed voltage of 32 Volts. The experiment was conducted at atmospheric pressure and room temperature in an enclosed chamber. DNT vapor was generated in a permeation oven by heating a 2-4 DNT permeation tube at constant temperature mixed with N_2 . The flow rates were controlled by mass flow controllers (MFC). Concentration of the DNT/ N_2 mixture can be adjusted by changing the flow rate and oven temperature (see Appendix B for

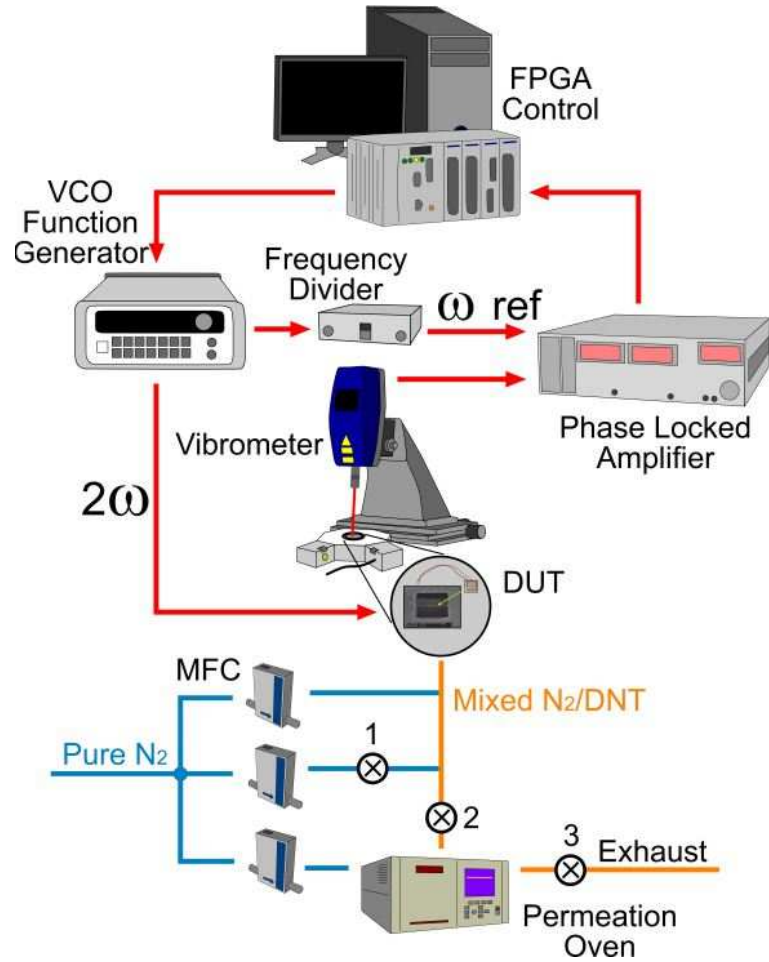


Figure 3.1: Experimental setup and FPGA controller design schematics. The device is mounted onto a shear piezo and is driven at twice its natural frequency. The sensor’s out of plane velocity response is coupled by a laser vibrometer through an optical microscope. The vibrometer signal and the reference square wave at half the drive frequency are fed into a phase lock amplifier (PLA). The FPGA samples the outputs of the PLA and provides feedback control to hold response close to the edge of bifurcation. The 2-4 DNT/ N_2 gas test experiment is conducted in a closed chamber at atmospheric pressure and room temperature. DNT/ N_2 is generated by heating the 2-4 DNT permeation tube in a permeation oven at constant temperature. DNT vapor is carried by N_2 and the mixture is fed into the test chamber at constant flow rate controlled by mass flow controllers. When the device is not under active DNT test, only N_2 is used.

detailed calculation of concentration). The sensor response was detected using a laser doppler vibrometer (LDV) through an optical microscope, although on-chip sensing using piezoresistors is possible at these scales [46]. The velocity signal was then sent to a phase lock amplifier (PLA). The PLA provided outputs that include the “in phase” component (X) of the signal, $V_{sig} \cos \phi$ and the “quadrature” component (Y), $V_{sig} \sin \phi$. They correspond to the sin and cos quadrature of the slow dynamic response of the system. The X and Y components were acquired by the FPGA controller at 250 kHz. Amplitude and phase information of the signal can be calculated from the X and Y data. Based on the statistics of the phase, the controller provides feedback to the function generator to perform corresponding frequency modulation to maintain the device close to the edge of bifurcation instability. The feedback controller was implemented on a National Instruments CompactRIOTM platform that contains FPGA input and output modules. It was invoked by the host VI to perform stand-alone tasks that will continue until either it is manually stopped or a bifurcation occurs. The FPGA sampled the X and Y components from the PLA at fixed loop rate of 250 kHz, limited by the maximum sampling frequency of the PLA. Phase and variance calculations are executed in parallel to the sampling loop. Based on the statistics of the phase and the phase variance set point, the FPGA output correspondingly increased or decreased the DC voltage to modulate the frequency of the function generator. The control rate can be tuned based on the variance set point, a threshold for control action. The rate was set at 1 ms. Predetermined knowledge of the natural frequency of the device is necessary to set

sensible parameters for the controller, so that the starting frequency is between the natural frequency of the sensor and its double. The drive frequency approaches the bifurcation until the phase noise squeeze state occurs (below the phase variance set point), then the controller actively controls the device at the edge of bifurcation and tracks its change as explosive gas is introduced.

Chapter 4

Results

Noise squeezing behavior was observed in the device under testing and matched the description in [27] and [28] when under no control action. To see how the sensor responded to the noise squeezing controller, data was collected when the controller was in action. X and Y data from the phase lock amplifier was collected from oscilloscope (DPO 2024) at a sampling rate of 625 kS/s and a data length of 1.25 million. The collected data was then analyzed in MATLAB. Phase was calculated by

$$\phi = \arctan \frac{Y}{X} \quad (4.1)$$

and amplitude was calculated by correlating the output voltage to sensitivity of the laser vibrometer. Phase variance was calculated from the most recent 100 samples. Note that for better visualization, data shown in Fig.4.1 is only one tenth of the collected data.

The highlighted portion of phase variance data in red is shown in an inset to get a closer look at the parameter of interest. As shown in Fig.4.1(a), when the device is away from the critical point, the phase varies between $-\pi$ to π , and the phase variance

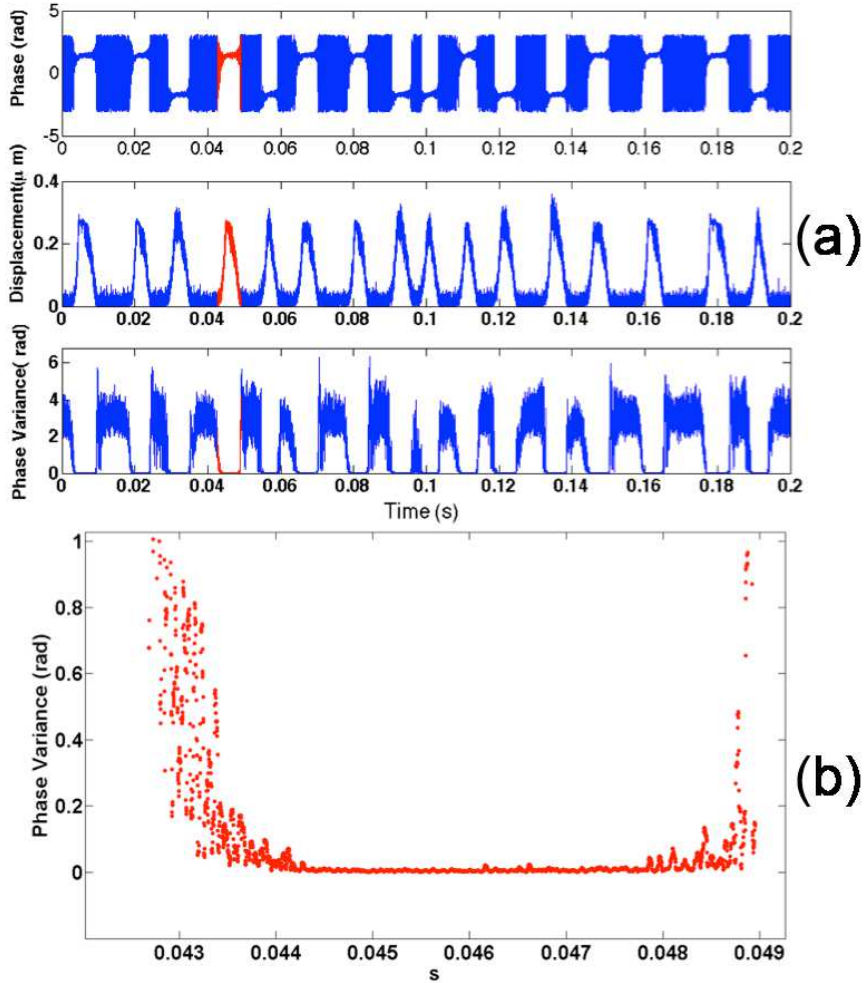


Figure 4.1: Sensor response to noise squeezing controller. Fig.4.1(a) shows the response of the sensor when noise squeezing controller is in action. When the sensor is away from the edge of instability, the phase is varying between $-\pi$ and π , and that corresponds to the zero stable solution of the supercritical pitchfork bifurcation. As the device approaches the edge of bifurcation, phase squeezes and amplitude starts to grow. When phase variance goes below threshold, the controller brings the sensor back to the stable state. Such process repeats and the time between one squeeze state and the next is less than 10 ms. Fig.4.1(b) is the phase variance data blow up of the highlighted portion in red in Fig.4.1(a). Minimum variance is found to be 0.002. This corresponds to the variance set point at which a feedback control was employed by adjusting the drive frequency to keep the device getting too close to the escape event.

is above 2 *rads*. This state corresponds to the zero stable solution of the pitchfork bifurcation. As the device approaches the edge of instability, the phase squeezes and the amplitude starts to grow. The phase variance drops to a minimum variance of 0.002. This apparent change in phase variance prior to the bifurcation event is the key to the feedback control. The cycle between one squeeze state to the next is less than 10 ms. 2-4 dinitrotoluene (2-4 DNT) gas sensing experiment was performed with the noise-squeezing controller at a low concentration of 0.93 parts-per-billion (ppb) DNT/N₂ mixture. In this experiment, nine repeated tests of 15 minutes of pure N₂ followed by 10 minutes of DNT/N₂ were conducted. Fig.4.2 shows the change of natural frequency as a function of time. Data in Fig. 4.2 has taken a linear frequency drift of 0.05 Hz/min into account. Higher concentration DNT gas experiments were also conducted. These

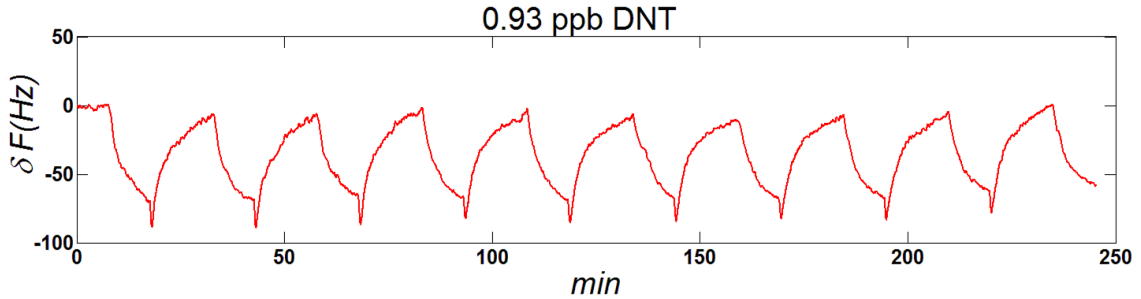


Figure 4.2: The figure shows a constant concentration of 0.93 ppb DNT/N₂ gas experiment. Pure N₂ was first introduced for 15 minutes and was followed 10 minutes of DNT/N₂. The parametric drive frequency was lowered by 67 ± 3 Hz due to the polymer absorption of DNT. The same process was repeated 9 times. The linear frequency drift of 0.05 Hz/min was accounted for in the post processing.

experiments were carried out by the noise squeezing bifurcation sensing method and the bifurcation sweep tracking method described in [12] for comparison, as shown in

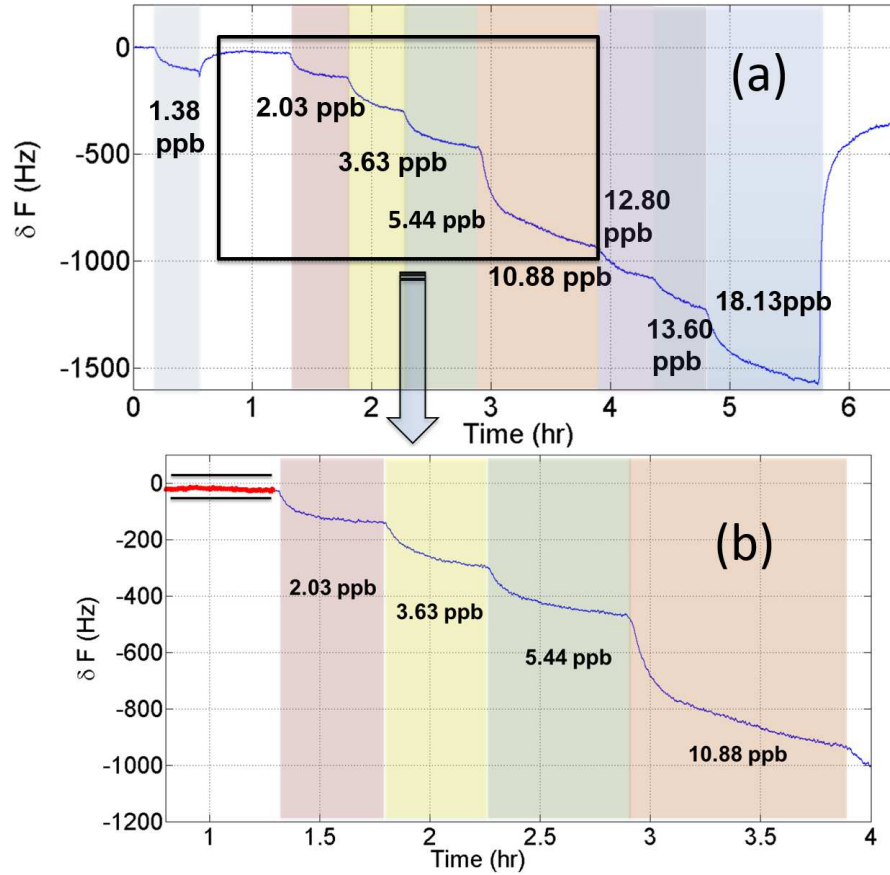


Figure 4.3: DNT gas sensing using a noise squeezing controller. Fig.4.3 (a) shows the gas experiment with lowest concentration of 1.38 ppb and highest concentration of 18.13 ppb. Fig.4.3(b) is a zoom in figure of the portion inside the square window in Fig.4.3(a). The highlighted portion corresponds to pure N_2 purging after the 1.38 ppb DNT/ N_2 gas test. However, absorbed DNT did not completely come off, and the frequency did not fully recover initial starting frequency. Hence, this explains why the highlighted data in red does not start at zero. Fig.4.3 (b) is used to make direct comparison with the data collected from the bifurcation sweep method (Fig.4.4) at the same concentration.

Fig.4.3 and Fig.4.4. Increasing concentration of DNT gas mixture was introduced after the steady state of the lower concentration of DNT testing was reached. Hence, after each cycle of DNT testing, no pure N_2 was used to release the absorbed DNT molecule. The motivation for this test came from the observation that the coatings would not fully recover following an N_2 purge. It was therefore necessary to understand potential

saturation effects. However, each higher concentration of DNT introduced results in a larger shift of natural frequency at saturation state in reference to initial state before introduction of any DNT. Hence, this experiment was valid in finding the absorption calibration curve for the sensor. Calibration curve of frequency shift as function of

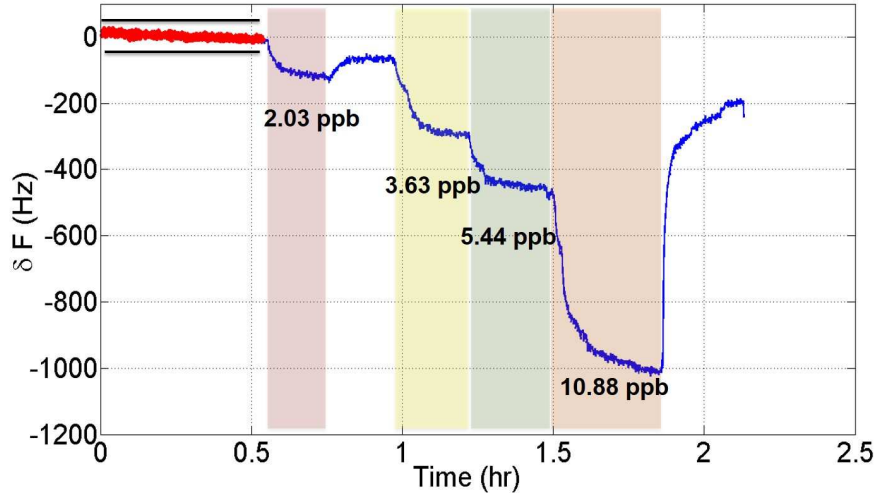


Figure 4.4: Comparison test showing DNT gas sensing using the bifurcation sweep method. Pure N_2 was introduced after the first and last DNT gas test (2.03 ppb and 10.88 ppb). Absorption phenomenon persisted, and the following higher concentration DNT/ N_2 experiments were conducted after the steady state of lower concentration was reached.

concentration is plotted in Fig.4.5 and the slope is a measure of the sensitivity of the MIPs response in the presence of DNT. Allan deviation [47] calculated as

$$\sigma = \sqrt{\frac{1}{2(n-1)} \sum_{j=2}^n (f_j - f_{j-1})^2} \quad (4.2)$$

was used to quantify the frequency stability of the highlighted portion of the data from the two tracking methods in Fig.4.3 and Fig.4.4. This corresponds to the minimum

frequency (minFreq) that can be detected. Slopes (sensitivity) of the calibration curve were fitted with a first-order polynomial. They are found to be 87.62 ± 3 Hz/ppb with

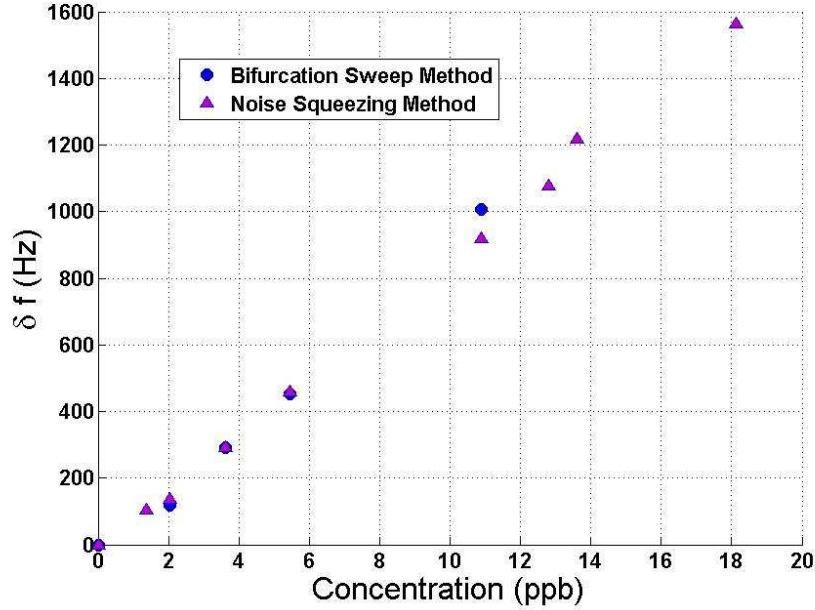


Figure 4.5: Calibration of DNT plotted with change of frequency as a function of DNT concentration using both tracking methods. The slope corresponds to sensitivity in units of Hz/ppb. The error bar is not shown in the figure, as it is invisible in the plot using the plot dot size shown.

R^2 of 0.9985 and 94.7 ± 13.5 Hz/ppb with R^2 of 0.9941 for noise squeezing bifurcation tracking and bifurcation sweep tracking correspondingly. Note that the frequency shift shown in all the figures in this work correspond to the drive frequency shift. Hence, to relate them to natural frequency shift, a multiplication factor of 0.5 is needed. The limit of detection (LOD) is calculated by $\text{minFreq}/\text{Sensitivity}$. The results are summarized in Table 4.1.

In gas sensing experiments, switching from DNT/ N_2 to pure N_2 caused a drop in frequency before rising. This was observed in both sensing strategies, shown in Fig.

4.6. It could be the results of the pressure change resulting from the manual switching of valves or sudden temperature change from DNT to N₂. However, it is most likely due to the energy dissipation when DNT molecules breaks the bonds with the MIP cavity, which leads to temperature change between the gas and polymer interface. The sensor is sensitive enough to capture this transient effect of the polymer interaction dynamics. In fact, using microcantilever to characterize energy absorption or dissipation in chemical reactions can be a potential new direction for research.

| | Noise Squeezing Method | Bifurcation Sweep Method |
|---------------------------|---------------------------|-----------------------------|
| Minimum Frequency (Hz) | 0.045 | 5.43 |
| Sensitivity (Hz/ppb) | 87.62 ± 3 | 94.7 ± 13.5 |
| LOD (ppb) | 0.0005 | 0.06 |

Table 4.1: Comparison of the two nonlinear tracking methods. This table summarizes the results of both the noise squeezing-based and bifurcation sweep-based methods. Minimum frequency corresponds to the Allan Variance for each method and the sensitivity relates to the slope of the calibration curve. LOD is the ratio between the minimum frequency and the sensitivity

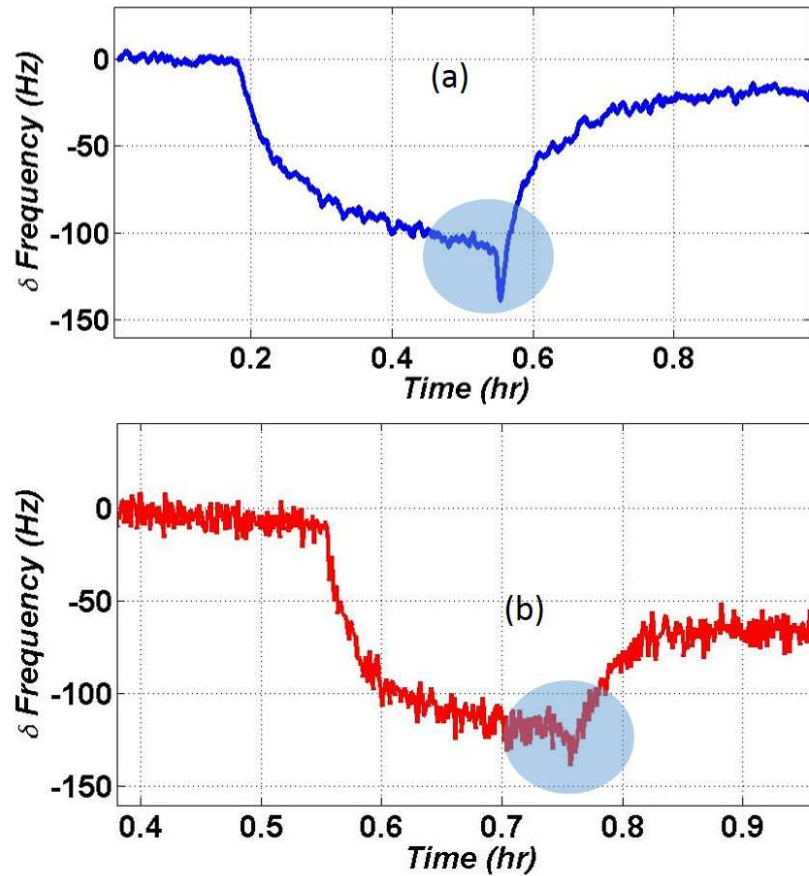


Figure 4.6: Transition from DNT gas testing to pure N_2 . Fig.4.6 (a) shows the 1.38 ppb DNT tracking using the noise squeezing controller and sharper transition is observed compared to the bifurcation sweeping method of 2.03 ppb in Fig.4.6 (b). Note that concentration is different in this figure; however, the focus on this result is not the frequency shift but the sensor response to the environmental change when switching the control valves on and off. Hence, the comparison is still valid despite being two different concentration tests.

Chapter 5

Discussion

Experimental results demonstrate that noise-squeezing control for bifurcation sensing is a better sensing strategy than the bifurcation sweep method previously described in [12]. It uses the statistics of the phase noise as a precursor to the bifurcation event, and the control time is less than 10 ms, as shown in Fig.4.1. The average time for a bifurcation sweep method to track a bifurcation event is 15 to 20 seconds, depending on sweep rate, since it takes time for oscillations to build. This method involves time for a system reset due to hysteresis and time for the sweep steps towards the critical point. And the sweep rate can result in delay bifurcation or activate escape if swept too fast or too slow. More than three orders of magnitude improvement in acquisition is achieved using the noise squeezing method for bifurcation detection. Since the phase squeezes onto the slow manifold before the bifurcation event takes place, and it possesses a more dramatic transition than the amplitude growth at this stage, it is a faster and more accurate approach to estimate the bifurcation location. The advantage of the noise squeezing method is evident in the frequency stability of the sensor, which is

over two orders of magnitude smaller than that of the bifurcation sweep method. This is significant because it means two orders improvement in ultimate sensitivity of the sensor. Furthermore, fast data acquisition employing the noise squeezing strategy not only results in higher confidence on the estimation of the bifurcation locations, but also enables more information on the response dynamics of the MIPs, as shown in Fig.4.6. As a result, the noise squeezing-based bifurcation tracking can be used for other applications in addition to mass sensing, for example, to characterize the absorption kinetics of MIP to further improve surface coating chemistry. The sharp transition between switching from DNT/N₂ to pure N₂ is likely due to the pressure change when one manually turns the gas valves on and off. Both methods capture the changes, however, the noise squeezing method captures more detail. The relatively slow bifurcation sweep method can result in an “aliasing effect”, where the sampling rate is slow compared to the rate of environmental change. It is obvious from the results that the noise squeezing controller offers more advantages in gas sensing than the previous bifurcation sweep method in the sense of frequency tracking mechanism, however, the sensor response time and reversibility did not improve compared to the results in [12]. The sensor response time to DNT from [12] is 90 seconds at a concentration of 1.8 ppb while it is found to be about 7 minutes at the lowest concentration tested (0.93 ppb, Fig.4.2). Moreover, absorption and stiction of DNT molecule during pure N₂ purging cycle was evident in Fig.4.6, where frequency stabilized below the initial frequency before DNT gas testing. However, it was not an issue in low concentration gas testing in Fig.4.2, where the

sensor demonstrated consistent repeatability and reversibility. Note that the sensor's sensitivity to the absorption of DNT is directly correlated to the surface coating chemistry. Hence, time response during DNT test is not an implication of the slow response from the controller or the MEMS device itself, since the absorption is characterized by the sensitivity of the MIPs. The differences in the results are likely due to degradation of the MIPs, since the sensors were coated over two years ago, which is also the duration between the experiment shown in [12] and the experiments conducted in this paper.

A direct comparison between the noise squeezing method and harmonic resonance method for tracking is not presented in this thesis. However, based on the previous work seen in [12][20][27], it has been shown that the natural frequency tracking results in lower frequency resolution in air as it is dependent on the quality factor, though it can be enhanced in high vacuum, it is not ideal for applications for mass sensing at atmospheric pressure. The limit of detection for this method is also limited by the measurement noise and thermo-mechanical sensor noise. In bifurcation tracking, despite the change in damping due to pressure has little effect on the sharpness and location of the parametric resonance, as seen in [27]. In addition, the frequency resolution is enhanced compared to harmonic resonance sensing in the presence of measurement noise [12]. Hence, one can be confident in the improvement of the noise squeezing sensing technique over the harmonic resonance tracking for mass detection in air.

Chapter 6

Conclusion

Experiments successfully demonstrate that noise squeezing based sensing is a superior sensing strategy over sweep-based bifurcation tracking methods for real time DNT explosive sensing at atmospheric pressure. Three orders of magnitude improvement in acquisition rate leads to faster, more confident and more precise estimation over the compared sensing method. The significant improvement in the minimum frequency resolution leads to lowest order of detection limit down to vapor concentrations of parts per trillion (ppt). Even though the sensor response to the TNT is slow due to the degradation of the MIPs, it does not question the sensitivity of the noise-squeezing controller, since the TNT/DNT sensitivity of the sensor is highly dependent on the sensitivity of the coating. Based on the positive results of the new sensing strategy applied to real-time sensing, a newly developed MIP-coating with better sensitivity, selectivity and stability will be used in a new set of microbeams and better sensor response is expected.

The advantage of using a microcantilever as a gas sensor is the feasibility of making it selective to vapors/particles of interest by functionalizing it with different coatings. Currently our collaborator from Army Research Laboratory(ARL) is working on a new type of MIP that provide good affinity for dimethyl methyl phosphate(DMMP), a common nerve agent stimulant. They are focusing on improving the MIP coating by optimizing the chemistry to better cover the surface of the microcantilevers and optimize the DMMP interaction. The effectiveness and absorption dynamics of the newly developed MIP can be characterized using noise squeezing bifurcation resonant tracking.

Furthermore, the system can be integrated into on-chip level sensing and actuation using piezoresistive and piezoelectric materials.

Chapter 7

Future Work

Thus far we have demonstrated parametric mass sensing by sweeping towards the bifurcation jump location and by tracking the edge of instability without actually bifurcating. But what about inside the Arnold tongue, where large stable solutions exist? Can we operate at some point along the bistable branch and track the change of the frequency shifts as the tongue moves? Absolutely – an amplitude control operating parametrically along the stable branch. Mass absorption or release will result in a change in Tongue location, and therefore, the shift of the stable branch(Fig.7.1). By actively controlling at constant amplitude through frequency modulation will allow us to trace the corresponding frequency shifts.

7.1 Choice of Control Locations

As seen in Fig.7.1, controller can be implemented at various amplitude control set point. Point A is closer to the wedge of instability, and the response amplitude rises at a steeper slope than anywhere else along the bistable branch. This location can be an

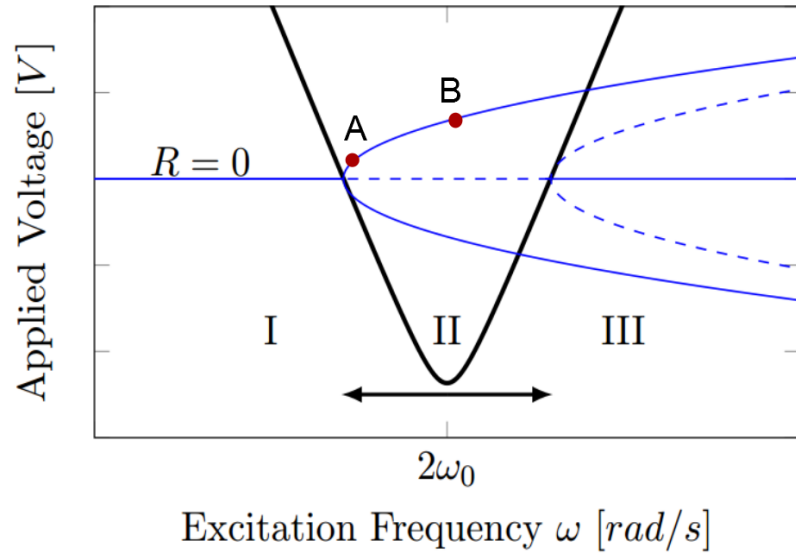


Figure 7.1: Control locations inside the Arnold Tongue. Point A and B are possible control set points. A is closer to the transition location where zero instability changes. At this point, the amplitude response along the bistable branch is steeper, which is likely to be more sensitive. B is further inside the tongue at a large amplitude, this location is less steep, but easier to control [2][1].

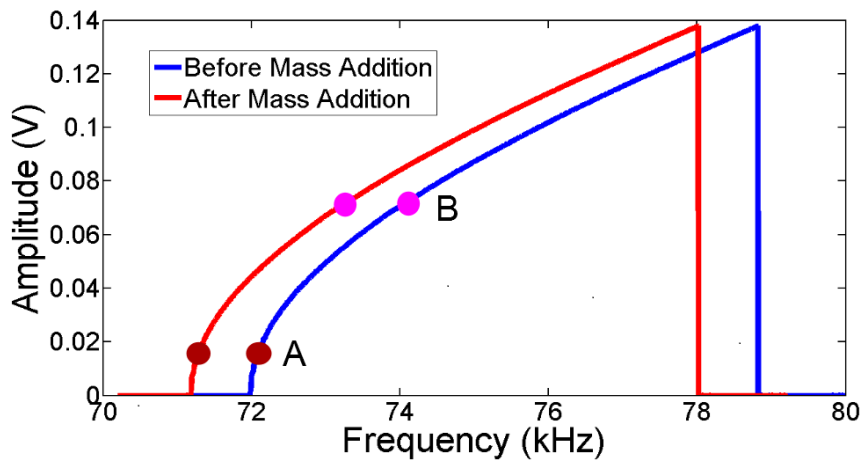


Figure 7.2: Illustration of how control set point A and B moves with the bistable branch in mass sensing experiment. Red and blue curve represent after and before mass absorption respectively.

ideal operation point for high sensitivity detection in mass sensing, since a small change in frequency can lead to significant change in amplitude. Point B is further inside the tongue at a higher amplitude. It is possible to control at B, and a PI controller would likely to be sufficient since the change of amplitude is more gradual than A.

7.2 Implementation of PI controller and its limitation

To demonstrate the ability of amplitude control application in mass sensing, we designed a simple PI controller and performed water vapor sensing experiment in atmospheric pressure. This controller is designed without the use of FPGA, which simplifies the electronics, however, FPGA can be implemented into the controller design in the future if speed becomes a limiting factor. Preliminary results with the PI controller demonstrated the capability of amplitude control in the application of mass sensing, as shown in Fig. 7.2. Reversibility and repeatability is validated with a water vapor experiment. The mass change in this experiment is 8.052 ng, and a standard deviation of the minimum frequency resolution is 0.52 Hz, corresponding to a lowest order of detection of 0.568 pg.

However, when controlling at an amplitude at point A, the controller fails to remain at A. Due to the sharp slope at point A, a small error results in a large gain, causing the control to loop around the set point, but it never converges. Hence, a more sophisticated

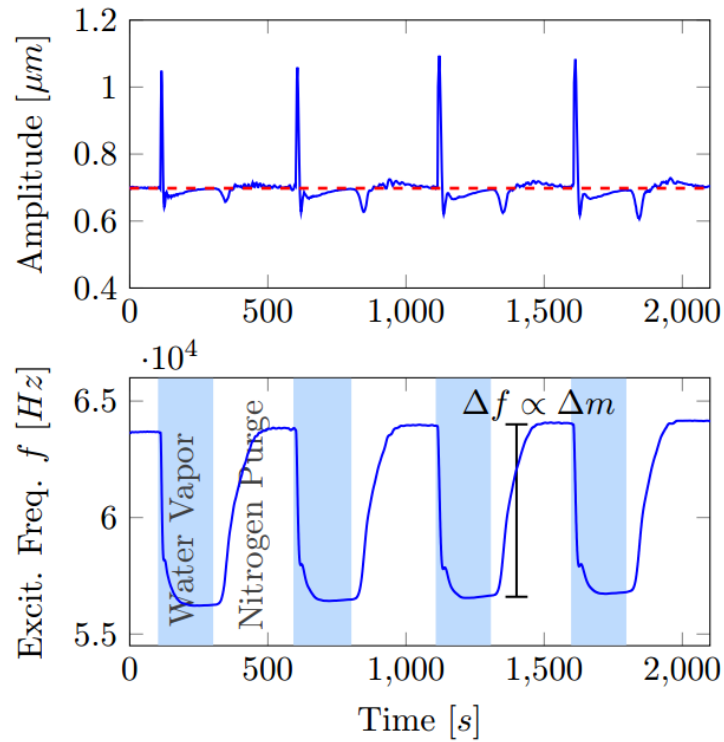


Figure 7.3: Water vapor experiment. *Top:* The controller actively controls the amplitude at set point (in red) by modulating the drive frequency. *Bottom:* When water vapor is introduced, natural frequency change of the sensor cause a shift of the tongue, and thus the stable branch. By controlling constant amplitude, the change in frequency is traced by the controller simultaneously. The change in mass Δm is directly related to Δf . The water vapor experiment is conducted by alternating water vapor and N_2 purging cycles. Reversibility and repeatability are demonstrated [2].

controller such as H_∞ control might be implemented. For such controller, careful system identification is necessary to determine coefficients such as damping, nonlinear stiffness and forcing strength. With these parameters identified, a linearized model can be used for the controller design. Currently this controller is being designed, and excellent agreement between the numerical simulation and the physical model based on [1] gives us great confidence of eventually having a working controller that will be able to operate and maintain constant amplitude at point A. The sensitivity is expected to be as good or better than the phase noise squeezing controller.

Bibliography

- [1] Tobias Hiller. System identification, design and implementation of a feedback-controller on a nonlinear MEMS mass sensor with parametric resonance. Master's thesis, University of Stuttgart, Germany, September 2014.
- [2] Lily Li, Tobias Hiller, and Kimberly Turner. Amplitude control of parametric resonances for mass sensing. *Proceedings of Sensors*, 2014 [in progress].
- [3] Zi Yie. *Exploiting Parametric Resonance and Amplification in Micro-cantilever-based Mass Sensing*. University of California, Santa Barbara, 2012.
- [4] Chris Burgner. *Noise in Nonlinear MEMS as it Applies to Sensing*. University of California, Santa Barbara, 2013.
- [5] Larry Senesac and Thomas G Thundat. Nanosensors for trace explosive detection. *Materials Today*, 11(3):28–36, 2008.
- [6] J Sarah Caygill, Frank Davis, and Seamus PJ Higson. Current trends in explosive detection techniques. *Talanta*, 88:14–29, 2012.

- [7] H P Lang, R Berger, F Battiston, J-P Ramseyer, E Meyer, C Andreoli, J Brugger, P Vettiger, M Despont, T Mezzacasa, et al. A chemical sensor based on a micromechanical cantilever array for the identification of gases and vapors. *Applied Physics A: Materials Science & Processing*, 66:S61–S64, 1998.
- [8] F M Battiston, J-P Ramseyer, H P Lang, M K Baller, Ch Gerber, J K Gimzewski, E Meyer, and H-J Güntherodt. A chemical sensor based on a microfabricated cantilever array with simultaneous resonance-frequency and bending readout. *Sensors and Actuators B: Chemical*, 77(1):122–131, 2001.
- [9] Cédric Ayela, Fanny Vandeveld, Denis Lagrange, Karsten Haupt, and Liviu Nicu. Combining resonant piezoelectric micromembranes with molecularly imprinted polymers. *Angewandte Chemie*, 119(48):9431–9434, 2007.
- [10] J A García-Calzón and M E Díaz-García. Characterization of binding sites in molecularly imprinted polymers. *Sensors and Actuators B: Chemical*, 123(2):1180–1194, 2007.
- [11] Ellen L Holthoff, Dimitra N Stratis-Cullum, and Mikella E Hankus. A nanosensor for tnt detection based on molecularly imprinted polymers and surface enhanced raman scattering. *Sensors*, 11(3):2700–2714, 2011.
- [12] K L Turner, C B Burgner, Z Yie, and E L Holthoff. Using nonlinearity to enhance micro/nanosensor performance. *IEEE Sens. Proc*, pages 154–157, 2012.

- [13] K L Ekinici, Y T Yang, and M L Roukes. Ultimate limits to inertial mass sensing based upon nanoelectromechanical systems. *Journal of applied physics*, 95(5):2682–2689, 2004.
- [14] Jeffrey F Rhoads, Steven W Shaw, Kimberly L Turner, Jeff Moehlis, Barry E DeMartini, and Wenhua Zhang. Generalized parametric resonance in electrostatically actuated microelectromechanical oscillators. *Journal of Sound and Vibration*, 296(4):797–829, 2006.
- [15] Jeffrey F Rhoads, Steven W Shaw, and Kimberly L Turner. The nonlinear response of resonant microbeam systems with purely-parametric electrostatic actuation. *Journal of Micromechanics and Microengineering*, 16(5):890, 2006.
- [16] Jeffrey F Rhoads, Steven W Shaw, and Kimberly L Turner. Nonlinear dynamics and its applications in micro-and nanoresonators. *Journal of dynamic systems, measurement, and control*, 132(3):034001, 2010.
- [17] Zi Yie, Nicholas J Miller, Steven W Shaw, and Kimberly L Turner. Parametric amplification in a resonant sensing array. *Journal of Micromechanics and Microengineering*, 22(3):35004–35010, 2012.
- [18] Andrew N Cleland. Thermomechanical noise limits on parametric sensing with nanomechanical resonators. *New Journal of Physics*, 7(1):235, 2005.
- [19] Rugar D. and Grutter P. Mechanical parametric amplification and thermomechanical noise squeezing. *Physical Review Letters*, 1991.

- [20] Zi Yie, Mark A Zielke, Christopher B Burgner, and Kimberly L Turner. Comparison of parametric and linear mass detection in the presence of detection noise. *Journal of Micromechanics and Microengineering*, 21(2):025027, 2011.
- [21] Franz J Giessibl. Atomic resolution of the silicon (111)-(7x7) surface by atomic force microscopy. *Science*, 267(5194):68–71, 1995.
- [22] Roberto Raiteri, Massimo Grattarola, Hans-Jürgen Butt, and Petr Skládal. Micromechanical cantilever-based biosensors. *Sensors and Actuators B: Chemical*, 79(2):115–126, 2001.
- [23] R Raiteri, H-J Butt, and M Grattarola. Changes in surface stress at the liquid/solid interface measured with a microcantilever. *Electrochimica Acta*, 46(2):157–163, 2000.
- [24] Nickolay V Lavrik, Michael J Sepaniak, and Panos G Datskos. Cantilever transducers as a platform for chemical and biological sensors. *Review of scientific instruments*, 75(7):2229–2253, 2004.
- [25] Laura G Carrascosa, M Moreno, Mar Álvarez, and Laura M Lechuga. Nanomechanical biosensors: a new sensing tool. *TrAC Trends in Analytical Chemistry*, 25(3):196–206, 2006.
- [26] KL Ekinici, XMH Huang, and ML Roukes. Ultrasensitive nanoelectromechanical mass detection. *Applied Physics Letters*, 84(22):4469–4471, 2004.

- [27] Wenhua Zhang and Kimberly L Turner. Application of parametric resonance amplification in a single-crystal silicon micro-oscillator based mass sensor. *Sensors and Actuators A: Physical*, 122(1):23–30, 2005.
- [28] Frédéric Lochon, Isabelle Dufour, and Dominique Rebière. An alternative solution to improve sensitivity of resonant microcantilever chemical sensors: Comparison between using high-order modes and reducing dimensions. *Sensors and Actuators B: Chemical*, 108(1):979–985, 2005.
- [29] Ali H Nayfeh and Dean T Mook. *Nonlinear oscillations*. John Wiley & Sons, 2008.
- [30] Leonard Meirovitch. *Principles and techniques of vibrations*, volume 1. Prentice Hall New Jersey, 1997.
- [31] Richard H Rand. Lecture notes on nonlinear vibrations. 2012.
- [32] S Neil Rasband. *Chaotic dynamics of nonlinear systems*, volume 1. New York, NY: Wiley, 1997.
- [33] Congzhong Guo, K M Shah, and G K Fedder. Electrically driven cmos-mems nonlinear parametric resonator design using a hierarchical mems circuit library. In *Solid-State Sensors, Actuators and Microsystems Conference (TRANSDUCERS), 2011 16th International*, pages 2402–2405. IEEE, 2011.
- [34] Congzhong Guo and Gary K Fedder. A quadratic-shaped-finger comb parametric resonator. *Journal of Micromechanics and Microengineering*, 23(9):095007, 2013.

- [35] Kimberly L Turner, Scott A Miller, Peter G Hartwell, Noel C MacDonald, Steven H Strogatz, and Scott G Adams. Five parametric resonances in a microelectromechanical system. *Nature*, 396(6707):149–152, 1998.
- [36] Michael V Requa and Kimberly L Turner. Precise frequency estimation in a microelectromechanical parametric resonator. *Applied Physics Letters*, 90(17):173508, 2007.
- [37] Chris Burgner, Nick Miller, Steve Shaw, and Kimberly Turner. Parameter sweep strategies for sensing using bifurcations in mems. In *Solid-State Sensor, Actuator, and Microsystems Workshop, Hilton Head Workshop*, 2010.
- [38] Michel H Devoret, Daniel Esteve, John M Martinis, Andrew Cleland, and John Clarke. Resonant activation of a brownian particle out of a potential well: Microwave-enhanced escape from the zero-voltage state of a josephson junction. *Physical Review B*, 36(1):58, 1987.
- [39] Mykhaylo Evstigneev. Statistics of forced thermally activated escape events out of a metastable state: Most probable escape force and escape-force moments. *Physical Review E*, 78(1):011118, 2008.
- [40] N G Stocks, R Mannella, and Peter V E McClintock. Influence of random fluctuations on delayed bifurcations. ii. the cases of white and colored additive and multiplicative noise. *Physical Review A*, 42(6):3356, 1990.

- [41] Paul Mandel and Thomas Erneux. The slow passage through a steady bifurcation: delay and memory effects. *Journal of statistical physics*, 48(5-6):1059–1070, 1987.
- [42] Gyan Prakash, Arvind Raman, Jeffrey Rhoads, and Ronald G Reifenberger. Parametric noise squeezing and parametric resonance of microcantilevers in air and liquid environments. *Review of Scientific Instruments*, 83(6):065109, 2012.
- [43] Nicholas Miller, Chris Burgner, Mark Dykman, Steven Shaw, and Kimberly Turner. Fast estimation of bifurcation conditions using noisy response data. In *SPIE Smart Structures and Materials+ Nondestructive Evaluation and Health Monitoring*, pages 76470O–76470O. International Society for Optics and Photonics, 2010.
- [44] C B Burgner, W S Snyders, and K L Turner. Control of mems on the edge of instability. In *Solid-State Sensors, Actuators and Microsystems Conference (TRANSDUCERS), 2011 16th International*, pages 1990–1993. IEEE, 2011.
- [45] C B Burgner, L A Shaw, and K L Turner. A new method for resonant sensing based on noise in nonlinear mems. In *Micro Electro Mechanical Systems (MEMS), 2012 IEEE 25th International Conference on*, pages 511–514. IEEE, 2012.
- [46] L Guillermo Villanueva, Rassul B Karabalin, Matthew H Matheny, Eyal Kenig, Michael C Cross, and Michael L Roukes. A nanoscale parametric feedback oscillator. *Nano letters*, 11(11):5054–5059, 2011.
- [47] David W Allan. Statistics of atomic frequency standards. *Proceedings of the IEEE*, 54(2):221–230, 1966.

Appendices

Appendix A

Fabrication Of Fixed-Fixed Beams

The fabrication process in recipe I involved wet KOH etching for the fixed-fixed beam is adopted from Dr. Zi Yie's dissertation [3]. However, an improved fabrication process is developed and executed, as shown in Recipe II. The following processes use SOI wafer with the following dimensions: 2 μm Si device, 1 μm burried SiO₂ and 520 μm Si handle.

A.1 Recipe I

1. Wet thermal oxidation (thickness 5000 Å)
 - 1050 °C for 48 min
2. PECVD SiN on backside (thickness 2000 Å)
 - Use program yie z01 (time = 22 min and 13.2 sec)
3. Remove SiO₂ on frontside

- Ultrasonic in acetone, isopropanol, DI water for 2 min each
- Cover backside with blue masking tape
- BHF etch for 7 min and 30 sec
- Remove blue masking tape
- Ultrasonic in acetone, isopropanol, DI water for 2 min each

4. Lithography on frontside

- Spin HMDS at 4000 rpm for 30 sec
- Spin SPR 510A at 4000 rpm for 30 sec
- Soft bake at 90 °C for 1 min
- Login to GCA 6300 Stepper: [10, 322] and use program ffbeams\1020
- Expose for 1.2 sec
- Post bake at 105 °C for 1 min

5. DRIE to define frontside features

- Use program yie_z01 (time = 90 sec)

6. Solvent clean

- Strip PR using PRX-127 at 80 °C for 1 hr
- Rinse in acetone, isopropanol, DI water for 2 min each

7. Lithography on backside

- Spin HMDS at 4000 rpm for 30 sec on frontside
 - Spin SPR 220-3 at 2500 rpm for 30 sec on frontside
 - Soft bake at 115 °C for 90 sec
 - Spin HMDS at 4000 rpm for 30 sec on backside
 - Spin SPR 220-3 at 2500 rpm for 30 sec on backside
 - Soft bake at 115 °C for 90 sec
 - Align backside transparency mask to frontside on Karl Suss MA 6
 - Expose for 45 sec
 - Post bake at 115 °C for 90 sec
 - Develop in AZ300MIF for 1 min
 - Rinse with DI water for 2 min
8. ICP etch to open the vias on backside
- Use program SiOVert (time = 3 min and 30 sec)
9. Solvent clean
- Strip PR using PRX-127 at 80 °C for 1 hr
 - Rinse in acetone, isopropanol, DI water for 2 min each
10. Apply ProTEK on frontside
- O₂ plasma descum frontside for 1 min

- Spin ProTEK primer at 1500 rpm (1000 rpm/s) for 60 sec
- Bake at 205 °C for 1 min
- Spin ProTEK B3 at 1500 rpm (1000 rpm/s) for 60 sec
- Bake at 140 °C for 2 min
- Spin ProTEK B3 at 1500 rpm (1000 rpm/s) for 60 sec
- Bake at 140 °C for 2 min
- Bake at 205 °C for 1 min

11. KOH etch on backside

- Prepare 20% KOH bath from 45% w/w stock solution (add 180 mL of KOH to 325 mL of DI water)
- Etch for 8 hr and 42 min or until backside Si is etched through

12. Solvent clean

- Rinse in acetone, isopropanol, DI water for 2 min each

13. BHF etch to release device

- BHF etch for 14 min or until fully released
- O₂ plasma descum frontside for 10 min

A.2 Recipe II

1. Clean particulate with nanostrip for 10 min
2. PECVD SiO₂ on backside (thickness $\sim 3 \mu\text{m}$)
 - Use standard HF oxide for 130 min
3. Clean particulate with nanostrip for 10 min
4. Lithography on fronside
 - Spin HMDS at 4000rpm for 30 sec
 - Spin SPR 955cm-0.9 at 3000 RPM for 30 sec
 - Soft bake at 95 °C for 60 sec
 - Login to GCA 6300 stepper:[10,322] and use program ffbeams \ w1020
 - Expose for 1.2 sec
 - Post bake at 110 °C for 60 sec
 - Develop in AZ300MIF for 1 min
 - Rinse with DI water for 3 min
5. DRIE Bosch process
 - Use the standard bosch process for 3 min. However, it is advised to do a test run to obtain approximate etch rate prior to this step.

6. Solvent clean

- Strip off PR using PRX-127 at 80 °C for 30 min
- Replace with a new bath of PRX-127 for another 30 min
- Rinse in acetone, isopropanol, DI water for 3 min

7. Lithography on backside

- Spin HMDS at 4000 rpm for 30 sec on backside
- Spin SPR220-3 at 2500 rpm for 30 sec on backside
- Soft bake at 115 °C for 90 sec
- Align backside to transparency mask to frontside on Karl Suss MA 6.
- Expose for 45 sec (hard contact, gap 35)
- Post bake at 115 °C for 90 sec
- Develop in AZ300MIF for 60 sec
- Rinse in DI water for 2 min

8. ICP etch to open the vias on backside

- Use SIOVERT program for 18 minutes etched

9. Remover backside PR

- Strip off PR using PRX-127 at 80 °C for 30 min

- Replace with a new bath of PRX-127 for another 30 min Rinse in acetone, isopropanol, DI water for 3 min
10. Apply thick PR on frontside
- Spin HMDS at 4000 rpm for 30 sec on backside
 - Spin SPR220-7 at 1500 rpm for 60 sec on backside
 - Soft bake at 115 °C for 90 sec
11. HCl dip to remove native oxide
- Mix HCL:DI (1:10)
 - Dip 30 seconds
 - Rinse in DI water for 3 min
12. DRIE 500 μm
- Use CAO_N_02 for 2 hour 46 min 30 sec. Characterization prior to this step to obtain etch rate is highly recommended
13. Remove resist
- Clean with acetone, isopropanol and DI water for 3 min each.
 - PRX-127 at 80 °C for 1 hr
 - New bath PRX-127 at 80 °C for 30 min
 - O₂ plasma ashing for 3 min

14. HF vapor etch burried oxide

- O2 descum front and backside for 3 min each
- Carry the wafer to HF vapor machine without contact of any polymer surfaces
- Leave wafer on top of three pin stand in HF machine
- Use Recepte No.3 for 5 cycles (300 sec/ cycle) rate:994 Å/min

15. Au Coating

- Use E-Beam No.3 (Temescal)
- Deposite 100Å Ti at 0.5 Å/sec
- Deposite 300Å Au at 0.5 Å/sec

Appendix B

DNT Concentration Calculation

The specifications of the 2-4 DNT permeation tube are shown in Table B.1, where P_o is the DNT vaporizing rate at T_o . MW is the molecular weight of 2-4 DNT.

| | P_o (ng/min) at T_o (°C) | MW (g/mol) | $K_o = \frac{22.40}{MW}$ |
|---------|------------------------------|------------|--------------------------|
| 2-4 DNT | 926 at 110 | 182.14 | 0.123 |

Table B.1: Specifications of 2-4 DNT permeation tube.

The DNT concentration can be calculated as follows:

1. Given P_o and T_o , the rate at temperature T can be estimated to be

$$P = 10^{\log_{10}(P_o) + 0.034(T - T_o)}, \tag{B.1}$$

where P is the new permeation rate at temperature T .

2. The concentration in parts-per-billion (ppb) is given by

$$C = \left(\frac{K_0 P}{F} \right) \times 1000 \quad (\text{B.2})$$

where F is the flow rate in sccm (standard cm^3/min)

As shown in the equation B.2, changing either the flow rate F or the oven temperature will change the concentration. In this work, concentration is altered by changing the flow rate, since this can be done much easier and faster than changing the oven temperature. For the concentrations mentioned in this work, the temperature and flow rate settings are as follows:

| T (°C) | F(sccm) | C (ppb) |
|--------|---------|---------|
| 70 | 5350 | 0.93 |
| 75 | 5350 | 1.38 |
| 80 | 5350 | 2.03 |
| 80 | 3000 | 3.63 |
| 80 | 2000 | 5.44 |
| 80 | 1000 | 10.88 |
| 80 | 850 | 12.80 |
| 80 | 750 | 13.60 |
| 80 | 600 | 18.13 |

Table B.2: Concentrations of DNT and its corresponding temperature and flowrate settings.

Appendix C

Method of Averaging and Steady State Solution

The steady state solution to the nonlinear Mathieu equation (Eq. 1.5) can be solved by the method of averaging. We begin with

$$m\ddot{y} + c\dot{y} + (k + \nu \cos 2\omega t)y + k_3y^3 = 0 \quad (\text{C.1})$$

Normalizing the above equation by m , we get:

$$\ddot{y} + \frac{c}{m}\dot{y} + \left(\frac{k}{m} + \frac{\nu}{m} \cos 2\omega t\right)y + \frac{k_3}{m}y^3 = 0 \quad (\text{C.2})$$

Let $\mu = \frac{c}{m}$, $\omega_o^2 = \frac{k}{m}$, $\lambda = \frac{\nu}{m}$ and $\gamma = \frac{k_3}{m}$. Then Eq.C.2 is simplified to the following:

$$\ddot{y} + \mu\dot{y} + (\omega_o^2 + \lambda \cos 2\omega t)y + \gamma y^3 = 0 \quad (\text{C.3})$$

Assume the response to the system to be periodic oscillations of the form:

$$y = y_1 \cos \frac{\omega t}{2} - y_2 \sin \frac{\omega t}{2}, \quad \frac{dy}{dt} = -\frac{\omega}{2}(y_1 \sin \frac{\omega t}{2} + y_2 \cos \frac{\omega t}{2}) \quad (\text{C.4})$$

Substitute C.4 into C.3. Then the individual term are written as follows:

$$\ddot{y} = h_1(t) = -\frac{\omega}{2}(\dot{y}_1 \sin \frac{\omega t}{2} + \frac{\omega}{2}y_1 \cos \frac{\omega t}{2} + \dot{y}_2 \cos \frac{\omega t}{2} - \frac{\omega t}{2}y_2 \sin \frac{\omega t}{2}) \quad (\text{C.5})$$

$$\mu \dot{y} = h_2(t) = -\mu \frac{\omega}{2}(y_1 \sin \frac{\omega t}{2} + y_2 \cos \frac{\omega t}{2}) \quad (\text{C.6})$$

$$\omega_o^2 y = h_3(t) = \omega_o^2(y_1 \cos \frac{\omega t}{2} - y_2 \sin \frac{\omega t}{2}) \quad (\text{C.7})$$

$$\gamma y = h_4(t) = \gamma(y_1 \cos \frac{\omega t}{2} - y_2 \sin \frac{\omega t}{2})^3 \quad (\text{C.8})$$

$$\lambda \cos \omega t y = h_5(t) = \lambda \cos \omega t (y_1 \cos \frac{\omega t}{2} - y_2 \sin \frac{\omega t}{2}) \quad (\text{C.9})$$

$$= \lambda(y_1 \cos \frac{\omega t}{2} - y_2 \sin \frac{\omega t}{2}) \quad (\text{C.10})$$

Expand h_5 , perform the trigonometric product identities and ignoring the nonsecular terms $(\sin \frac{\omega t}{2}, \cos \frac{\omega t}{2})$. Then from C.3, we get $\sum_n h_n(t) = 0$. By summing the effect of each $h(t)$ and averaging it over one period of oscillation $T = \frac{4\pi}{\omega}$, we get:

$$\frac{1}{T} \int_0^T (\sum_n h_n(t)) \sin \frac{\omega t}{2} dt = 0 \quad (\text{C.11})$$

$$\frac{1}{T} \int_0^T (\sum_n h_n(t)) \cos \frac{\omega t}{2} dt = 0 \quad (\text{C.12})$$

Expand each coefficients in the *sin* quadrature:

$$\frac{1}{T} \int_0^T h_1(t) \sin \frac{\omega t}{2} dt = \langle h_1 \sin \frac{\omega t}{2} \rangle = -\frac{1}{2} \left(\frac{\omega}{2} \dot{y}_1 - \left(\frac{\omega}{2} \right)^2 y_2 \right) \quad (\text{C.13})$$

$$\langle h_2 \sin \frac{\omega t}{2} \rangle = -\mu \frac{\omega}{4} y_1 \quad (\text{C.14})$$

$$\langle h_3 \sin \frac{\omega t}{2} \rangle = -\frac{\omega_o^2 y_2}{2} \quad (\text{C.15})$$

$$\langle h_4 \sin \frac{\omega t}{2} \rangle = -\gamma \frac{3}{8} y_2 (y_1^2 + y_2^2) \quad (\text{C.16})$$

$$\langle h_5 \sin \frac{\omega t}{2} \rangle = \frac{\lambda y_2}{4} \quad (\text{C.17})$$

And the *cos* quadrature:

$$\frac{1}{T} \int_0^T h_1(t) \cos \frac{\omega t}{2} dt = \langle h_1 \cos \frac{\omega t}{2} \rangle = -\frac{1}{2} \left(\left(\frac{\omega}{2} \right)^2 y_1 - \frac{\omega}{2} \dot{y}_2 \right) \quad (\text{C.18})$$

$$\langle h_2 \cos \frac{\omega t}{2} \rangle = -\mu \frac{\omega}{4} y_2 \quad (\text{C.19})$$

$$\langle h_3 \cos \frac{\omega t}{2} \rangle = \frac{\omega_o^2 y_1}{2} \quad (\text{C.20})$$

$$\langle h_4 \cos \frac{\omega t}{2} \rangle = \gamma \frac{3}{8} y_1 (y_1^2 + y_2^2) \quad (\text{C.21})$$

$$\langle h_5 \cos \frac{\omega t}{2} \rangle = \frac{\lambda y_1}{4} \quad (\text{C.22})$$

Summing all the terms in *sin* and *cos* quadrature respectively, we get the governing equation for the slow variables.

$$\dot{y}_1 = -\mu y_1 + 2\Omega y_2 + \frac{\lambda}{\omega} y_2 - \frac{3\gamma}{2\omega} y_2 (y_1^2 + y_2^2) \quad (\text{C.23})$$

$$\dot{y}_2 = -\mu y_2 - 2\Omega y_1 + \frac{\lambda}{\omega} y_1 + \frac{3\gamma}{2\omega} y_1 (y_1^2 + y_2^2) \quad (\text{C.24})$$

where $\Omega = \frac{\omega}{2} - \omega_o$, defined as the detuning parameter of the system. The steady state solution can be solved by setting $\dot{y}_1 = \dot{y}_2 = 0$. Assume amplitude to be R , the y_1 and y_2 are related to R as:

$$y_1 = R \cos(\theta) \quad (\text{C.25})$$

$$y_2 = R \sin(\theta) \quad (\text{C.26})$$

$$R^2 = y_1^2 + y_2^2 \quad (\text{C.27})$$

Substitute C.25 and C.26 into C.23 and C.24 at steady state:

$$0 = -\mu y_1 + \left(\frac{\lambda}{\omega} + 2\Omega - \frac{3\gamma}{2\omega} R^2\right) y_2 \quad (\text{C.28})$$

$$0 = -\mu y_2 + \left(\frac{\lambda}{\omega} - 2\Omega + \frac{3\gamma}{2\omega} R^2\right) y_1 \quad (\text{C.29})$$

Plugging y_1 or y_2 from one equation to the other, we then reach the followings:

$$0 = \left(\frac{\lambda}{\omega}\right)^2 - \left(2\Omega - \frac{3\gamma}{2\omega}R^2\right)^2 - \mu^2 y_1^2 \quad (\text{C.30})$$

$$0 = \left(\frac{\lambda}{\omega}\right)^2 - \left(2\Omega - \frac{3\gamma}{2\omega}R^2\right)^2 - \mu^2 y_2^2 \quad (\text{C.31})$$

Then adding the two equations together gives:

$$\left(\frac{\lambda}{\omega}\right)^2 - \left(2\Omega - \frac{3\gamma}{2\omega}R^2\right)^2 - \mu^2 R^2 = 0 \quad (\text{C.32})$$

Solving the above equation and we get the expression for R :

$$R = \pm \sqrt{\frac{4\omega_0}{3\gamma} \left[2\Omega \pm \sqrt{\left(\frac{\lambda}{2\omega_0}\right)^2 - \mu^2} \right]} \quad (\text{C.33})$$

The above result is valid when $\omega \simeq 2\omega_0$, hence it can be expressed as $\omega = 2\omega_0 + \epsilon\omega_1$, with $\epsilon \ll 1$. Other averaging techniques such as two variable expansion method can also be used to find the steady state solution [1][31].

The system dynamics in the y_1 and y_2 quadrature can be transformed into polar coordinates through C.25 – C.27 and substituting them into C.23 and C.24. Taking derivatives of C.25 and C.26, we get:

$$\dot{y}_1 = \dot{R} \cos(\theta) - R \sin(\theta) \dot{\theta} \quad (\text{C.34})$$

$$\dot{y}_2 = \dot{R} \sin(\theta) + R \cos(\theta) \dot{\theta} \quad (\text{C.35})$$

After substitution and regrouping terms, with $\omega \simeq 2\omega_o$, we arrive at:

$$\dot{R} = -\mu R + \frac{R\lambda}{2\omega_o} \sin(2\theta) \quad (\text{C.36})$$

$$\dot{\theta} = -2\Omega + \frac{3R^2\gamma}{4\omega_o} + \frac{\lambda}{2\omega_o} \cos(2\theta) \quad (\text{C.37})$$